National Ignition Facility laser performance status

C. A. Haynam,* P. J. Wegner, J. M. Auerbach, M. W. Bowers, S. N. Dixit, G. V. Erbert, G. M. Heestand, M. A. Henesian, M. R. Hermann, K. S. Jancaitis, K. R. Manes, C. D. Marshall, N. C. Mehta, J. Menapace, E. Moses, J. R. Murray, M. C. Nostrand, C. D. Orth, R. Patterson, R. A. Sacks, M. J. Shaw, M. Spaeth, S. B. Sutton, W. H. Williams, C. C. Widmayer, R. K. White, S. T. Yang, and B. M. Van Wonterghem

Lawrence Livermore National Laboratory, P. O. Box 808, Livermore, California 94551

*Corresponding author: haynam1@llnl.gov

Received 7 December 2006; accepted 8 January 2007;
posted 22 January 2007 (Doc. ID 77868); published 15 May 2007

The National Ignition Facility (NIF) is the world's largest laser system. It contains a 192 beam neodymium glass laser that is designed to deliver 1.8 MJ at 500 TW at 351 nm in order to achieve energy gain (ignition) in a deuterium–tritium nuclear fusion target. To meet this goal, laser design criteria include the ability to generate pulses of up to 1.8 MJ total energy, with peak power of 500 TW and temporal pulse shapes spanning 2 orders of magnitude at the third harmonic (351 nm or 3ω) of the laser wavelength. The focal-spot fluence distribution of these pulses is carefully controlled, through a combination of special optics in the 1ω (1053 nm) portion of the laser (continuous phase plates), smoothing by spectral dispersion, and the overlapping of multiple beams with orthogonal polarization (polarization smoothing). We report performance qualification tests of the first eight beams of the NIF laser. Measurements are reported at both 1ω and 3ω, both with and without focal-spot conditioning. When scaled to full 192 beam operation, these results demonstrate, to the best of our knowledge for the first time, that the NIF will meet its laser performance design criteria, and that the NIF can simultaneously meet the temporal pulse shaping, focal-spot conditioning, and peak power requirements for two candidate indirect drive ignition designs. © 2007 Optical Society of America

OCIS codes: 140.0140, 140.3610, 140.3070.

1. Introduction

A. Facility Overview

The National Ignition Facility (NIF) is the world's largest laser system. It is designed to achieve the ignition of a deuterium–tritium (DT) nuclear fusion target. As of November 2006, the facility is 89% complete, and project completion is planned for the spring of 2009. NIF's 192 laser beamlines are housed in a building with a volume of ~350,000 m^3 (see Fig. 1). Each laser beamline is composed of 36 to 38 large-scale optics, depending on beamline configuration, (see Fig. 2) and hundreds of smaller optics, yielding a total area of ~3600 m^2 for all of the NIF's optics. The total near-field area of all 192 laser beams is ~22 m^2. For indirect-drive fusion studies, all 192 beams are focused into a cylindrical hohlraum through two circular entrance holes that are each ~2.5 mm in diameter (see Fig. 3). The conditions created in the hohlraum or in other targets will provide the necessary environment to explore a wide range of high-energy-density physics experiments, including laboratory-scale thermonuclear ignition and burn.

For the past decade, up to 1000 engineers, scientists, technicians, and skilled laborers have worked on the NIF. Over 2300 vendors have participated. Most of its necessary infrastructure is complete. As of November 2006, 40 of the 192 beamlines have been operated at the fundamental 1.053 μm wavelength (1ω) at ≥19 kJ/beamline, demonstrating a current facility 1ω capability of more than 750 kJ. Four beamlines have been delivered to the NIF target chamber and frequency converted to 351 nm light (3ω). This paper summarizes the results of perfor-

0003-6935/07/163276-28$15.00/0

Fig. 1. NIF is approximately 150 m × 90 m and seven stories tall. The roof of the building has been removed from this aerial photo, and an engineering rendering of the laser is shown. The two laser bays are shown on the upper-left portion of the figure. The switchyard (in red) is shown on the lower-right side, as is the spherical target chamber (in silver), into which the 192 beamlines converge.

mance qualification (PQ) tests conducted on the first bundle of eight beams in 2005 to 2006. We also discuss some earlier four-beam experiments conducted in 2003 to 2004, which explored the NIF laser operation in more detail. Recent tests in early 2006 utilized the precision diagnostics system (PDS) and culminated in shots that simultaneously achieved the

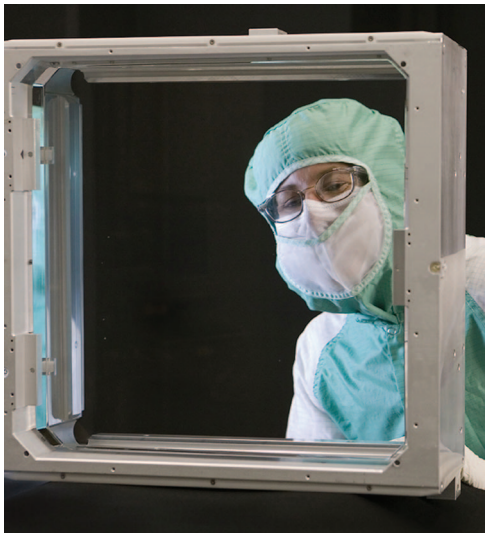

Fig. 2. (Color online) NIF's large optics each have an area of approximately 40 cm × 40 cm. The optic shown is a 7.7 m focal length wedged lens used to focus one beam onto the target. The lens shown was used during the campaigns discussed in this paper. This photograph was taken after this lens was exposed to 11 shots with between 8 and 9.4 kJ of 351 nm light (equivalent to between 1.6 and 1.8 MJ of 351 nm light for the full 192 beam NIF).

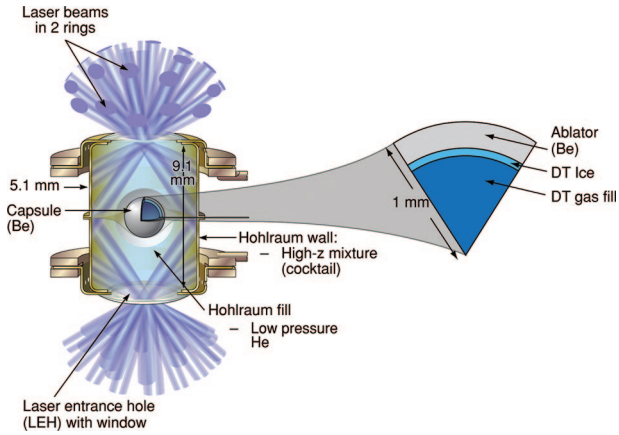

Fig. 3. (Color online) All of the 192 NIF laser beams are schematically shown focused into a single cylindrical hohlraum. Each cone shown in the figure is composed of four individual beams. The hohlraum is approximately 10 mm long by 5 mm in diameter. The laser entrance hole is ~2.5 mm in diameter. Each laser beam will be pointed to a precise location on the hohlraum wall and will generate x rays that will then drive the implosion of the central 1 mm radius spherical fusion capsule. The ensuing nuclear reaction is expected to release over 10 MJ of energy.

full per beam energy, peak power, pulse-shaping range and finesse, and focal-spot conditioning for which the NIF laser was designed. They verify that, when completed, the full facility will be able to produce the laser drive required to perform a wide variety of high-energy-density experiments, including compressing DT capsules to densities $>1000\ \mathrm{g/cm^3}$ for the inertial fusion ignition campaign.

B. Laser Overview

We summarize the laser design very briefly here. See Refs. [1–10] and the further references in those papers for detailed information. The performance of a physics prototype for the NIF laser, Beamlet, was described in this journal several years ago [11]. References [12–16] discuss the laser energies and pulse shapes required for various ignition targets.

The NIF laser pulse starts in a cw Yb-fiber master oscillator. From here it passes through an array of fiber-optical components to provide temporal amplitude and bandwidth control, and is split to drive 48 preamplifier modules located under the transport spatial filter of the main laser (see Fig. 4). This injection laser system (ILS) will be discussed in more detail in Section 3.

Immediately following the ILS, ~1% of the laser energy is diverted to a diagnostic suite known as the input sensor package (ISP). Here, the total energy, temporal shape, and near-field spatial shape from each preamplifier module (PAM) is measured [4]. The ILS can fire roughly one shot every 20 min. ISP measurements are important for both validating and normalizing our numerical models of the laser performance and for assuring that the ILS is properly configured prior to a main laser shot.

Pulses from the ILS are split four ways, supplying each of four main beamlines with energy that is adjustable from millijoules to more than a joule. Figure 4 shows a schematic of a single beamline of the main laser system. The pulse from the ILS is injected near the focal plane of the transport spatial filter (TSF). It expands to the full beam size of 37.2 cm × 37.2 cm (at the level of 0.1% of the peak fluence) and is collimated by the spatial filter lens. It then passes through the power amplifier (PA), reflects from a mirror and polarizer, and enters the cavity spatial filter (CSF). It traverses the main amplifier (MA), reflects off a deformable mirror that is used to correct wavefront distortions, and then goes through the MA and CSF again. By the time it makes this second pass through the CSF, a plasma-electrode Pockels cell (PEPC) switch has been fired to rotate the beam polarization by 90°, allowing it to pass through the polarizer and be reflected back for another double pass through the CSF and main amplifier. When it returns to the PEPC, the cell has switched off, so it now reflects from the polarizer, and passes a second time through the PA and TSF. After the TSF, a beamsplitter reflects a small sample of the output pulse back to the central TSF area, where it is collimated and directed to an output sensor package (OSP) located underneath the TSF. OSP diagnostics record the beam energy, temporal pulse shape, and near-field profiles [4]. The main pulse proceeds to the switchyard where four or five transport mirrors direct it to one of a number of final optics assemblies (FOAs) symmetrically located about, and mounted on, the target chamber. Each FOA contains a 1ω vacuum window, focal-spot beam-conditioning optics, two frequency conversion crystals to reach 351 nm wavelength, a focusing lens, a main debris shield that also serves as a beam diagnostic pickoff to measure energy and power, and a 1–3 mm thick disposable debris shield. The debris shields are used to protect the optics from target debris.

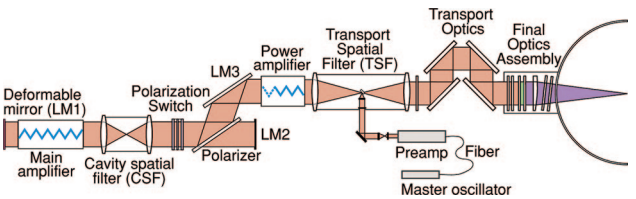

Fig. 4. (Color online) Schematic of one of the 192 beamlines in the National Ignition Facility. The laser's path through the optics is discussed in the text.

For the experiments reported in this paper, the beam was not transported to the target chamber. Instead, an array of either seven or eight calorimeters was inserted at the output of the TSF to both measure and absorb the 1ω laser energy. When the eighth calorimeter was absent, it was replaced by a pickoff that routed that beam to a suite of diagnostic instruments called the PDS, which is described in Appendix A. PDS has an extensive suite of diagnostics for 1ω, 2ω, and 3ω light. The PDS instruments can diagnose one beamline in great detail, whereas the OSP diagnostics (described in Appendix B) can acquire 1ω data on all 192 beams during a shot. In PDS, the laser was frequency converted to the second or third harmonic using typical NIF final optics. Diagnostics in the PDS allowed detailed study of the 1ω beam entering the FOA and the 1ω, 2ω, and 3ω beams exiting it.

The MA contains 11 Nd-glass laser slabs. The PA is configured to have as many as seven slabs, but typically contains five. Some NIF shots have had one, three, or seven slabs in the PA to explore the full range of operating conditions. As an indication of scale, the CSF is 22 m long, the TSF is 60 m, the path length from the TSF output to the target chamber is 60–75 m, and the target chamber is 5 m in radius.

The results presented in this paper cover the predicted and measured performance of the laser obtained during the final stages of the activation or commissioning of the first of the NIF's 24 bundles. The performance envelope of the 1ω portion of the laser was explored by a series of shots taken at progressively higher 1ω energies. In Section 2, we compare model predictions of each of the eight beamlines with measured energies, report the shot-to-shot energy reproducibility, and show the 1ω power and energy operating envelopes for the NIF. The 3ω power and energy envelope, measured in PDS, is also shown in this section.

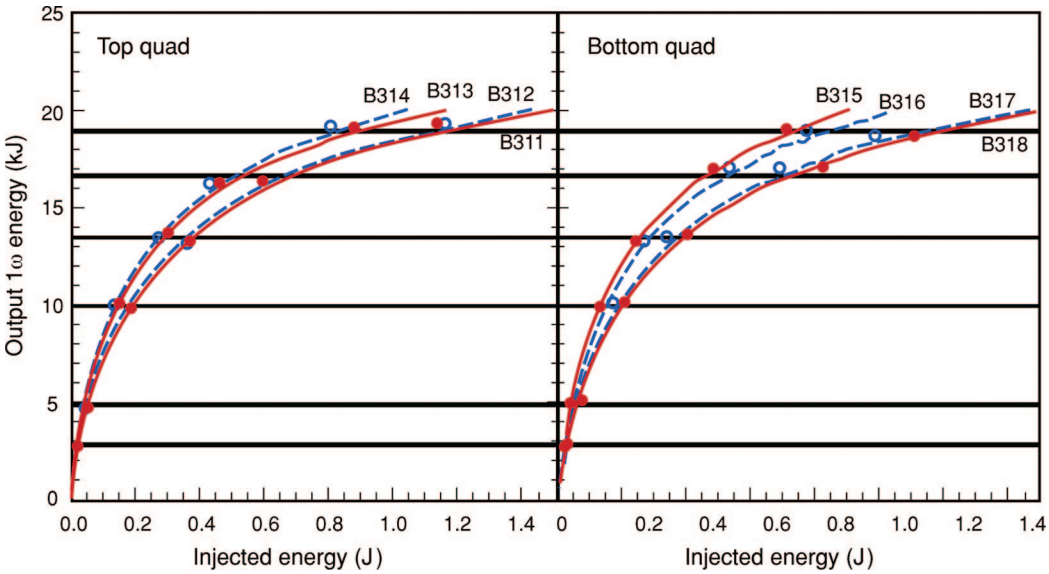

Fig. 5. (Color online) Comparison of modeled (dashed and solid curves) and measured (open and solid circles) energies for eight shots on Bundle 31. The output energy is measured by the full aperture calorimeters.

Section 3 details how a shaped pulse is created, diagnosed, amplified, and frequency converted as it traverses the NIF laser. It also describes a series of laser shots that validated the NIF's capability of meeting its energy, power, and temporal contrast design goals. These PQ shots were taken with an entire bundle operating at 1ω and with a single beamline delivered to the PDS, frequency converted, and diagnosed at 1ω, 2ω, and 3ω.

Section 4 describes the addition of focal-spot beam conditioning to the laser. It details the generation of two shaped pulses that have three beam-conditioning methods applied, while simultaneously generating the single-beam 3ω powers and energies planned for the first ignition campaigns on the NIF. The appendices of this paper cover the details of our laser model and the design and capabilities of the PDS.

2. Bundle Performance at 1ω and National Ignition Facility Operating Envelopes at 1ω/3ω

Each of the NIF's eight-beam laser bundles undergoes a 1ω operational qualification (OQ) and PQ before being used in any experiments. The OQ-PQ consists of firing eight to ten shots, using all eight beams, into a bank of full aperture calorimeters. These calorimeters measure absolute beam energy and calibrate a system of diodes in the OSP that serve as energy diagnostics during routine operations. Beam energies at 1ω for these shots range from 1 to 19 kJ, and pulse shapes are either flat in time (FIT) at the output or shaped to match user specifications. Besides verifying the bundle performance, these shots are used to calibrate and validate the laser performance operations model (LPOM) description of these beamlines, as described in Appendix C. The LPOM is then used to predict laser performance and to set up the ILS for all NIF shots.

A. LPOM Calibration Results

Figure 5 shows the comparison between modeled performance using the LPOM and energy measurements for eight shots on the first bundle of the NIF laser. In this figure, output 1ω energy refers to the energy measured at the output of the main laser with the full aperture calorimeters. The OSP was calibrated to these calorimeters. The injected energy is inferred from the ISP measurements, the known four-way ILS beam-split ratios, and the known transmission from the ISP to the injection at the TSF. The LPOM's predictions differ from the measurements by no more than 1.2%, demonstrating that the LPOM can be used to set the desired energy from each beamline accurately over an extended range of operations.

Table 1. Analysis of the 1ω Beam Energetics of Four Identical 19 kJ Shots

Shot Sequence Number	Desired 1ω Energy (kJ)	Average Measured Beamline 1ω Energy	Total Bundle 1ω Energy (kJ)	Deviation of Average from Desired (%)	Standard Deviation of Beamline Energies from Mean (%)
1	19.02	19.20	153.6	+0.98	0.84
2		19.15	153.2	+0.68	0.94
3		19.11	153.9	+0.50	0.67
4		19.10	153.8	+0.43	0.89

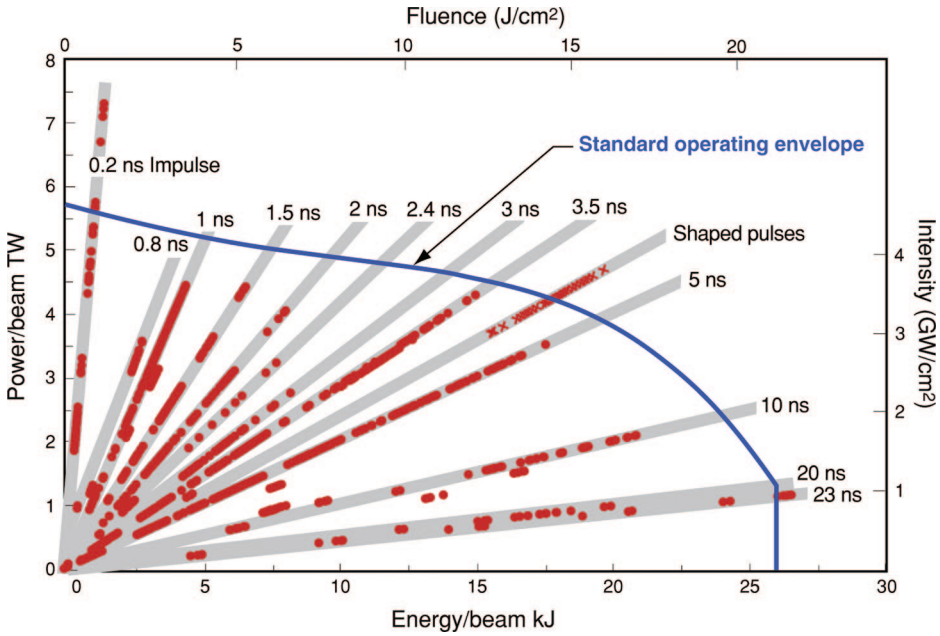

Fig. 6. (Color online) Plot of 1ω peak power per beam versus 1ω energy per beam for initial NIF shots. The dark solid curve is the LPOM's "equipment protection" operating limit.

The laser 1ω output energy is required to be reproducible to within 2% rms from shot to shot for proper ignition target performance. To test this performance criterion, the 19.2 kJ shot in Fig. 5 was repeated three times. After the first shot, no adjustments were made to either the injected pulse shape or the energy. As Table 1 shows, agreement with the target energy, the rms spread in total energy among the four shots, and the standard deviation of the eight beamline energies in each shot were all better than 1%. The estimated error in the 19.2 kJ energy measurement is 1.4% or 0.27 kJ. This error estimate is a root sum square (rss) sum of the observed random component (1.3%) and the known systematic uncertainty (0.42%) of the NIST calibration standard used in calibrating the NIF's calorimeters.

B. Power versus Energy Operating Envelopes for the National Ignition Facility

A system shot is defined as any event in which the flashlamps are fired in a bundle with all of the bundle's main laser (1ω) optics installed. Since commissioning

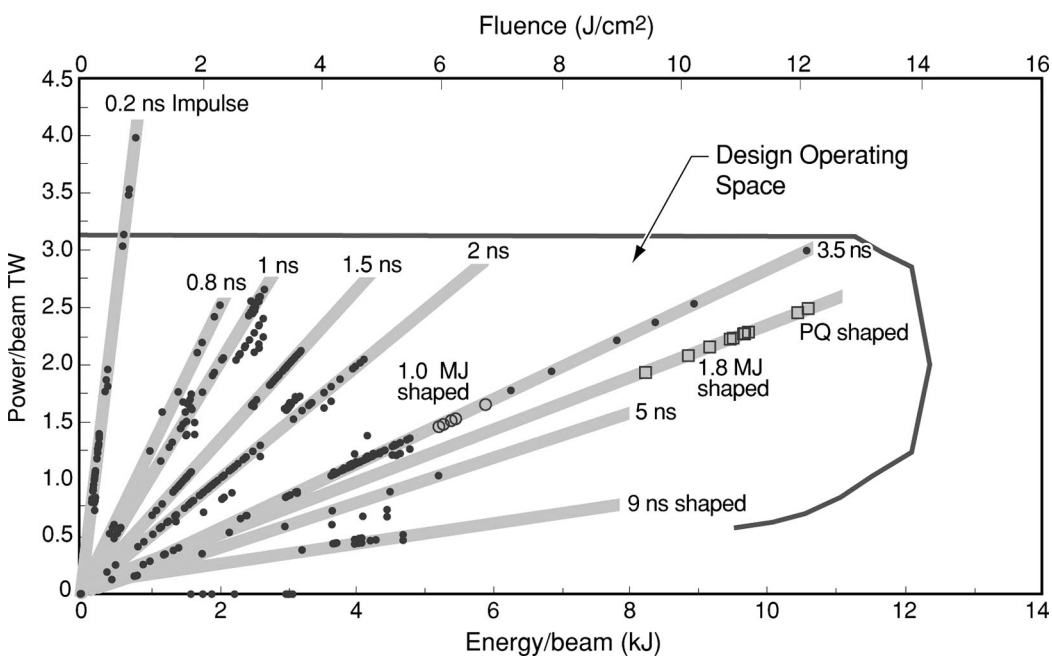

Fig. 7. Plot of 3ω beam power versus 3ω beam energy for initial NIF shots.

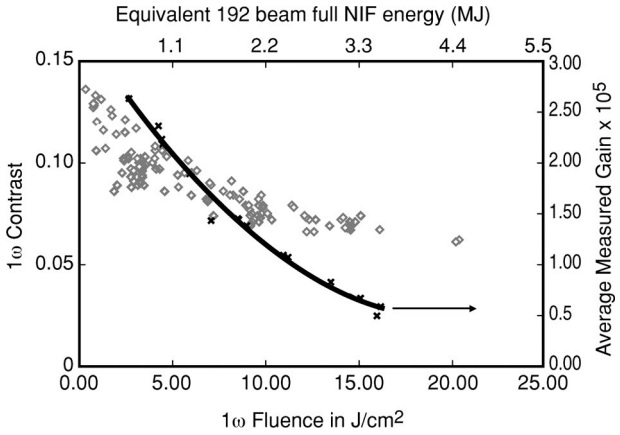

Fig. 8. Near-field fluence of 1ω beam contrast (diamonds) versus 1ω fluence, measured at the converter input in PDS. These points represent shots covering the 1ω operating range, and pulse lengths, as shown in Fig. 6. Also shown, as a solid curve, is the measured amplifier gain versus fluence showing that the contrast drops as the gain saturates.

the first four NIF beamlines in April 2001, the NIF has fired over 600 system shots. Figure 6 shows a summary of the 1ω shots fired together with the NIF standard 1ω operating envelope as currently set in the LPOM. This envelope does not represent the absolute limits of operation, as one can see from the several shots that lie above the limit, but rather a guide for routine operations. In general, the limit for high-power operation is set by the growth of small-scale intensity irregularities due to the nonlinear index in glass. For high-energy operation, the limit is determined by the injected energy available from the ILS.

Figure 7 similarly summarizes all 3ω shots since 2001. This 3ω performance space includes shaped pulses that meet or exceed the energy and power levels required for the current ignition target design. The NIF design operating range predicted [7] in 1994 is also plotted on this figure. These initial 3ω shots, combined with the validation of our LPOM projections over the range of shots shown, indicate that we can achieve the design power versus energy range as described in 1994.

High-power operation of previous Lawrence Livermore National Laboratory (LLNL) Nd-glass laser systems was limited by small-scale beam breakup [11,17], driven by the nonlinear index of the transmissive optics in the beam path. Small-scale contaminants or optics imperfections lead to beam intensity modulations. At high intensity, these modulations are amplified and focused by the nonlinear index effect. An early sign of the development of this instability is growth in the beam contrast, defined as the standard deviation of

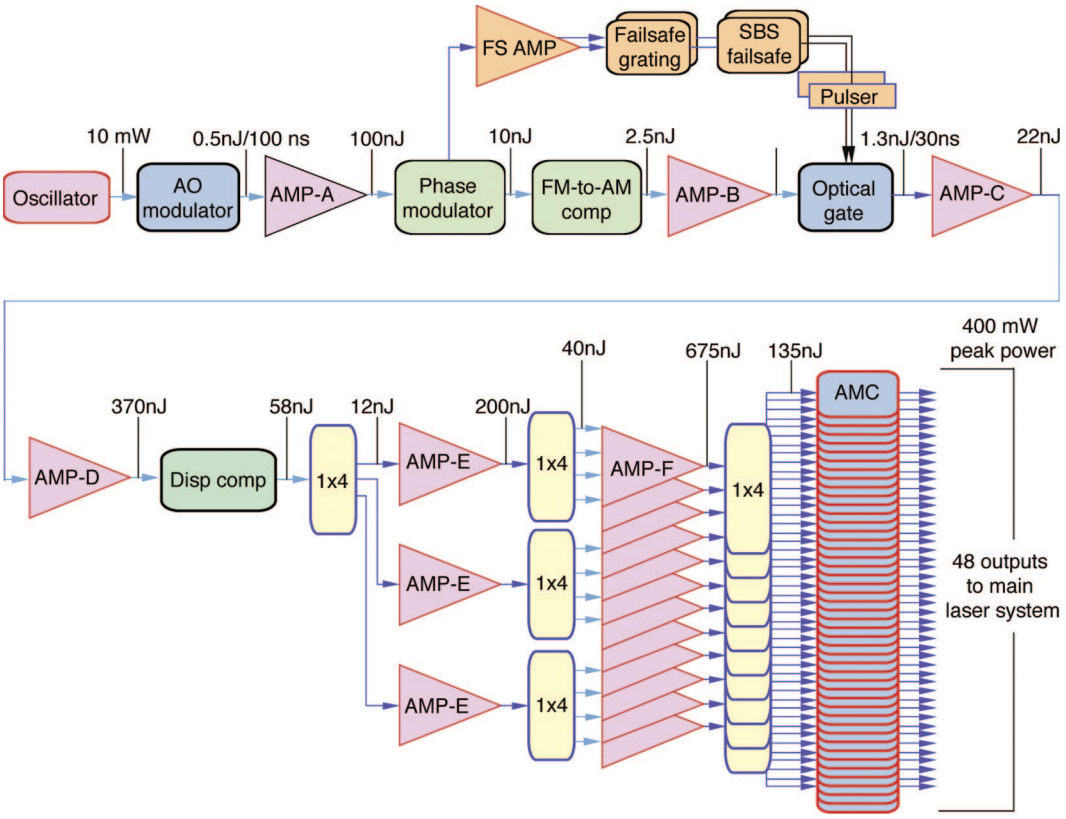

Fig. 9. (Color online) Schematic and power and/or energy levels of the master oscillator and NIF pulse-shaping system. Fiber amplifiers (triangles) are used to compensate for optical losses as the initial cw beam is chopped by the acousto-optic modulator, frequency broadened to 30 GHz bandwidth by the phase modulator, precompensated by the FM-to-AM compensator (to minimize amplitude modulation of the high-power beam), corrected for group-velocity dispersion in the dispersion compensator, then split, and finally temporally shaped in the AMC. The components shown produce the shaped pulse for all of the NIF's 48 preamplifier modules.

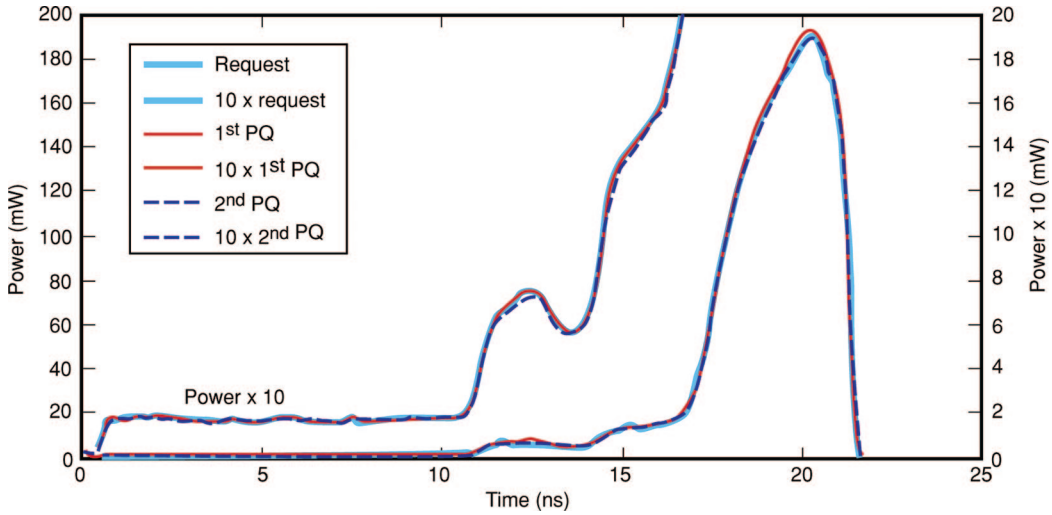

Fig. 10. (Color online) Temporal pulse shape at the output of the MOR for the two PQ shots designated as first PQ (N060329-002-999) and second PQ (N060329-003-999). The pulse shape was measured with a 1 GHz transient digitizer.

the fluence divided by its mean value. Contrast is measured by taking a sample of the near-field beam, projecting it on a camera, and calculating the fluence variation as recorded in the $m \times n$ camera image.

$$\text{Fluence beam contrast} \equiv \sqrt{\frac{1}{nm}\sum_{i=1}^{m}\sum_{j=1}^{n}\left(\frac{F(x_i, y_j) - \bar{F}}{\bar{F}}\right)^2},$$

$$F(x_i, y_j) = \text{pixelated fluence from near-field camera image,}$$

$$\bar{F} = \text{average fluence of image.} \quad (1)$$

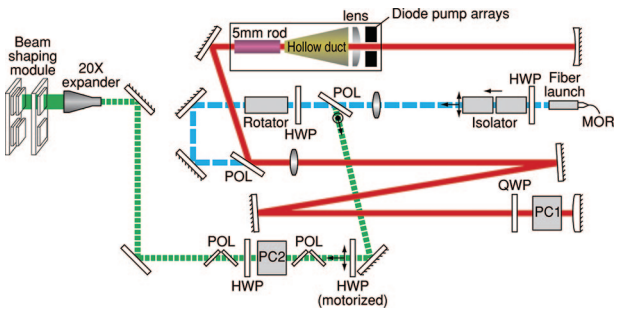

Fig. 11. (Color online) Schematic of ILS regenerative amplifier. Light enters the amplifier from the MOR fiber launch at the right of the figure (long-dashed line). It is collimated, passed through an optical isolator, and injected through a polarizer into the main regenerative amplifier cavity (solid line). After passing through the Pockels cell (PC1) once, the PC is switched on, trapping the pulse in the cavity for approximately 30 round trips. During each round trip, the pulse passes twice through a diode pumped rod amplifier. Prior to the final pass, the PC is switched off, and the light exits through a second polarizer (short-dashed line). A motorized half-wave plate in combination with a set of polarizers controls the energy transmitted to the next stage of amplification. A second Pockels cell (PC2) can be used to clip off a trailing portion of the pulse that is meant to saturate the regenerative amplifier for energy stability, but is not required in the rest of the laser. A 20× beam expander in combination with a beam-shaping module sculpts the beam to the desired spatial shape (solid line on left).

Figure 8 demonstrates that the NIF contrast at the input to the frequency converter consistently decreases with increasing fluence and energy per beam. The contrast reported here is calculated over the central 27 cm × 27 cm of the laser, measured with a NIF output camera. The decrease seen is a simple consequence of gain saturation: high-fluence regions in the beam experience less net gain than low-fluence regions, tending to decrease any intensity modulation. The data in Fig. 8 span the NIF design operating space, indicating that the careful attention we have paid to optical quality throughout the beamlines [2] has successfully controlled beam breakup.

3. Performance Qualification Shots for Ignition Target Pulse Shapes

In March of 2006, we fired two 3ω PQ shots separated by 3 h and 18 min. This interval is significantly shorter than the NIF design requirement of ≤8 h between system shots. Shot intervals of less than 4 h have been repeated on a regular basis during the commissioning of the first 40 NIF beamlines, with no discernable degradation in either beam wavefront or near-field modulation.

These PQ shots were taken to validate the NIF's capability to meet its energy, power, and temporal contrast design goals. One beam from each of these shots was routed to the PDS. The other seven beams were measured in the 1ω calorimeters. We will follow the performance of the laser, as measured by the diagnostics, through the four sections of the laser, starting with the 1ω sections [master oscillator room (MOR), PAM, and main laser] and finishing with the 3ω diagnostics following the FOA. A detailed discussion of the PDS diagnostics can be found in Appendix A. Appendix B describes the main laser diagnostics and the calorimeters.

A. Master Oscillator and Pulse-Shaping System

The MOR and pulse-shaping system (Fig. 9) creates the temporal pulse shape specified by the LPOM. The

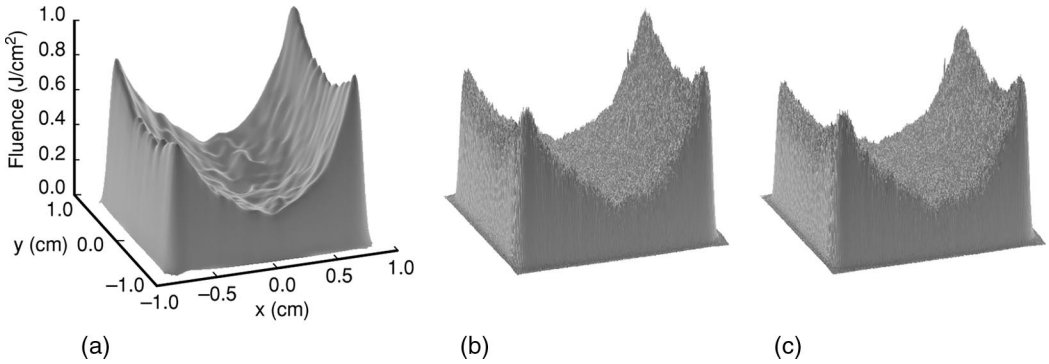

Fig. 12. Predicted (left) and measured, near-field profiles for the first (center) and second (right) performance qualification shots.

LPOM determines a MOR temporal pulse shape that compensates for gain saturation in the rest of the 1ω laser and for power dependence of the frequency converter efficiency, so that the desired 3ω pulse shape is achieved.

The pulse begins in a cw Yb-fiber master oscillator tuned to 1.053 μm wavelength. The cw signal from the output of the oscillator is chopped by an acousto-optic modulator to a pulse width of 100 ns at a pulse repetition rate of 960 Hz. The light is phase modulated at a frequency of 3 GHz to a total bandwidth of 30 GHz in order to suppress stimulated Brillouin scattering (SBS) in the main laser optics [18]. A high-reliability fail-safe system is in place to guarantee that the pulse cannot proceed beyond the MOR unless adequate modulation has been applied to assure that SBS will be suppressed [8]. A separate modulator operating at 17 GHz can apply more than 150 GHz additional bandwidth at 1ω (450 GHz at 3ω) for beam smoothing by spectral dispersion (SSD), as will be discussed in Subsection 4.B. The pulse next transits a cascade of fiber splitters and Yb-fiber amplifiers culminating in 48 fiber outputs each of ~1 nJ energy. Each output goes into an amplitude modulator chassis (AMC) that sets the pulse shape for injection into a PAM.

There are 48 AMCs, each of which independently provides the pulse to drive the corresponding PAM and its associated four main beamlines. A digital oscilloscope immediately following the AMC records its pulse shape. The AMC controller averages a few hundred individual pulses, calculates the deviation of that average from the requested pulse shapes, and then uses a negative feedback loop to minimize this deviation. Figure 10 compares the requested and measured pulse shapes for the two performance qualification shots.

B. Preamplifier Module Description and Performance

Each of the 48 pulses from the MOR enters the main laser bay on an optical fiber and is injected into a PAM, where it is amplified first by a regenerative amplifier system and then by a four-pass rod amplifier [8–10]. This is shown schematically in Fig. 11. The pulse makes ~30 round trips in the regenerative amplifier experiencing a gain that raises its energy from ~1 nJ to ~20 mJ, as appropriate for each PAM. After being switched out of the regenerative ampli-

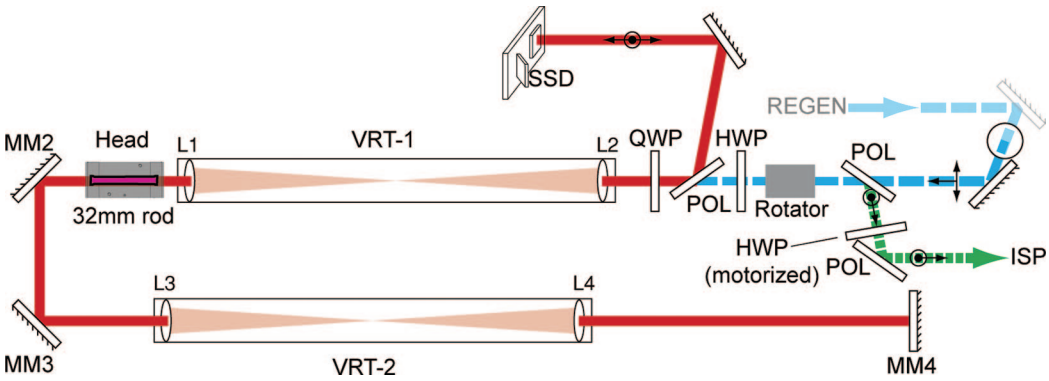

Fig. 13. (Color online) Schematic of the MPA system. Light enters from the regenerative amplifier at the right of the figure (long-dashed line), and transmits through the polarizer. The polarization is rotated by a series of half-wave plates and quarter-wave plates (HWPs and QWPs) so that the pulse passes four times through the 32 mm flashlamp-pumped rod amplifier (solid line) before exiting through the polarizer. Each pass is optically relayed using a set of two vacuum relay telescopes (VRT). These VRTs are evacuated to prevent air breakdown at the central focus of the telescope. As the pulse exits the cavity (short-dashed line), it passes through a combination of a motorized HWP and a polarization-sensitive mirror to allow control of the energy transmitted to the PABTS and the main laser.

Table 2. Requested and Measured Energies at the Input and Output of the MPA

	MPA Input Energy (mJ)	MPA Output Energy (J)
Requested	1.41	1.11
First PQ shot	1.40	1.09
First PQ deviation (%)	−0.7	−2
Second PQ shot	1.40	1.02
Second PQ deviation (%)	−0.7	−8

fier, the pulse traverses a spatial shaping module that transforms the Gaussian spatial shape to a profile that is designed to compensate for the spatial nonuniformity of the gain throughout the rest of the laser. Figure 12 compares the predicted spatial profile at the ISP location to measurements from the two PQ shots. The ability to accurately shape the spatial profile allows the NIF to produce beams at the output of the system that have a flat irradiance distribution across the central part of the beam.

After passing through the beam-shaping module in the PAM, the pulse is injected into the multipass amplifier (MPA), which is shown schematically in Fig. 13. The beam makes four passes though the amplifier rod in the MPA, yielding a nominal net energy gain of 1000. The overall energy gain of the ILS is of the order of 10^9. LPOM uses both off-line and on-line data analysis to maintain ILS models that have the accuracy needed to predict the energetics of this high-gain system. Table 2 shows a comparison of the modeled and measured energies at the input and output of the MPA for both PQ shots.

The input energy to the MPA is monitored at 1 Hz. It is maintained at the requested value by a closed-loop control using attenuation provided by the combined action of an adjustable half-wave plate and a polarizer used in transmission. The closed-loop control mechanism produces energies within ±2% of the request. The LPOM's MPA model is accurate to within ±5% for injected energies ranging from 0.5 to 10 mJ. Figure 14 shows a comparison of the predicted and measured ISP power sensor traces for the two PQ shots.

C. Main Laser 1ω Performance

After the ISP, the pulse is injected into the main laser—the part of the laser system that contains the full-aperture (40 cm) components. The near-field and far-field spatial and temporal profiles at the 1ω output of the main laser are modeled using the NIF virtual beamline (VBL) propagation code, which has been incorporated into the LPOM, as described in Appendix C. The LPOM contains detailed information regarding sources of wavefront distortion. All large optics undergo full-aperture, high-resolution interferometer measurements during their manufacture. The interferometry data are used directly in the LPOM description for each optic at the position in the chain where the optic is located. The distortion induced as the laser slabs are deformed by nonuniform flashlamp heating has been both calculated and measured; calculated aberrations are used in the LPOM. Calculated estimates for distortions due to mounting stresses and a contribution for air turbulence in the amplifier cavities are also included. Finally, a model of the 39-actuator, full-aperture deformable mirror, using measured influence functions for each actuator, is also used to represent the correction done on line in the Hartmann sensor—deformable mirror loop.

High spatial frequency wavefront errors generate corresponding high spatial frequency intensity variations in the measured beam profile. Lower spatial frequency wavefront errors (less than ~0.1/mm) affect spot size, not near-field intensity, because laser propagation distances are insufficient for them to diffract into intensity variations. The lower spatial fre-

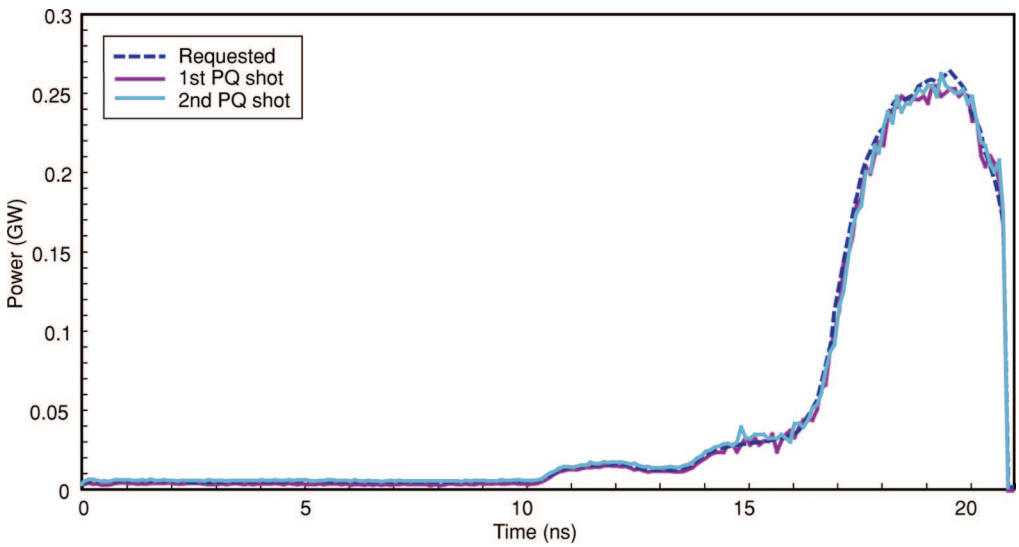

Fig. 14. (Color online) Requested and measured temporal profiles at the output of the preamplifier module (prior to injection into the main laser) as measured by the ISP for the two PQ shots.

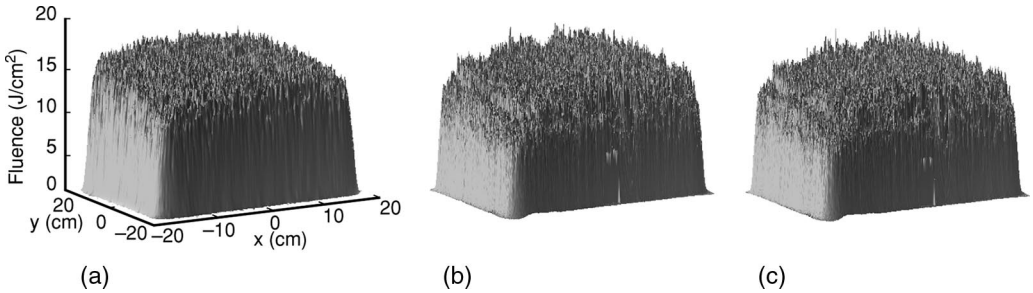

Fig. 15. Comparison of (a) modeled and measured near-field 1ω fluence distributions at PDS for the (b) first and (c) second PQ shots, respectively.

quency variations in the near-field measurements are caused primarily by the input spatial shape, gain spatial profiles, and aberrations in the laser front end.

Figure 15 compares the measured and modeled near fields at the 1ω PDS near-field camera position for both PQ shots. These shots had a 1.8 MJ ignition-target pulse shape (discussed below under temporal pulse shaping) and 1ω energy of ~18 kJ per beam. Figure 16 shows an overlap of the measured and modeled fluence probability distributions over the central 27 cm × 27 cm of the beam. The first PQ shot had a slightly higher energy than the second (18.0 kJ compared with 17.6 kJ, due to an adjustment to the injected energy). Agreement between the measured and modeled contrast is sufficient for the LPOM to specify laser energetics and pulse shapes, protecting against equipment damage caused by off-normal laser operation. The <0.5% absolute discrepancy in contrast may arise from sources such as small inaccuracies in the modeled gain spatial shape (overall flatness of the beam), approximations made in the statistical modeling of front-end optic aberrations, or the calculational estimate made of the contrast added by the diagnostic optics. The measured values of 1ω contrast are well below the NIF design goal of ≤10%.

Figure 17 displays plots of the enclosed fraction of the focal-spot energy as a function of radius, starting at the centroid of the spot. Two measurements are shown for each PQ shot. The first was taken directly from the PDS 1ω far-field camera. The second used the measured wavefront from the 1ω radial shear interferometer and fluence from the near-field camera. From these two inputs, the beam field was numerically reconstructed and a far field predicted. Both the LPOM and the radial shear predictions are at paraxial focus (simple Fourier transform of the field) and are in good agreement. Both, however, predict somewhat smaller focal spots than the direct measurements. The most likely explanation is that our diagnostic imaged a location that was slightly displaced from best focus (1 to 2 mm out of 7700 mm). Figure 18 shows the spatial fluence profile of the calculated and measured focal spots. The shot-to-shot

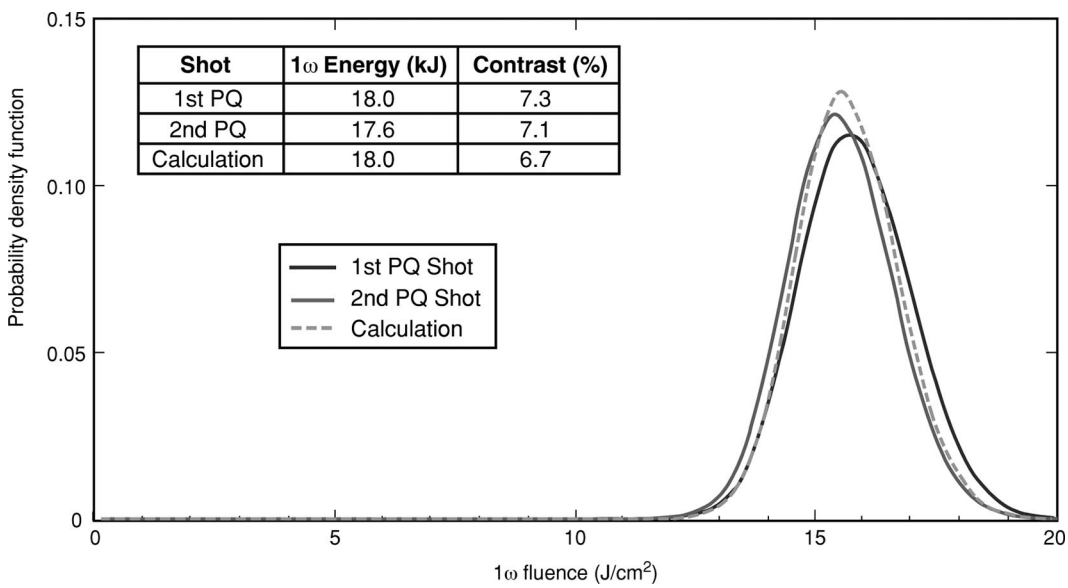

Shot	1ω Energy (kJ)	Contrast (%)
1st PQ	18.0	7.3
2nd PQ	17.6	7.1
Calculation	18.0	6.7

Fig. 16. Comparison of modeled and measured fluence probability distributions at the PDS 1ω diagnostic, over the central 27 cm × 27 cm of the beam, for the two PQ shots. The small shifts in mean 1ω fluence are due to differing total energies in the two PQ shots. The calculation is reported at the mean fluence of the two PQ shots over the central 27 cm × 27 cm of the beam. Measured contrast is nearly identical for both shots, in reasonable agreement with prediction, and well under our design goal of 10%.

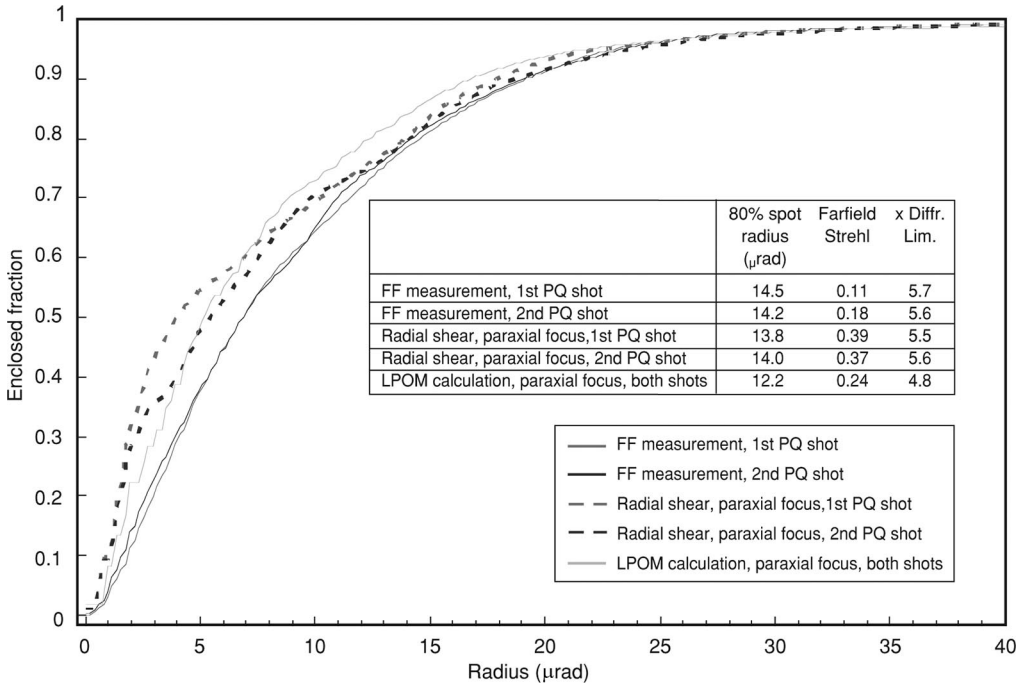

	80% spot radius (μrad)	Farfield Strehl	x Diffr. Lim.
FF measurement, 1st PQ shot	14.5	0.11	5.7
FF measurement, 2nd PQ shot	14.2	0.18	5.6
Radial shear, paraxial focus,1st PQ shot	13.8	0.39	5.5
Radial shear, paraxial focus, 2nd PQ shot	14.0	0.37	5.6
LPOM calculation, paraxial focus, both shots	12.2	0.24	4.8

Fig. 17. Enclosed 1ω focal-spot energy fractions for measurement and calculation of the two PQ shots. Both direct far-field measurements and predictions based on reconstruction of the field using the radial shear and near-field diagnostics are shown. The calculated far field applies to both shots.

variability is minor as demonstrated by the small change in the 80% spot radius (see Fig. 17).

D. Frequency Conversion Performance

The target must be irradiated with 351 nm light. The NIF converts the main laser output pulse to the third harmonic using a pair of KDP frequency conversion crystals as illustrated [19,20] in Fig. 19. The first crystal, or doubler, converts approximately two thirds of the incident laser energy to the second harmonic via type-I phase-matched degenerate sum-frequency mixing: $1\omega(o) + 1\omega(o) \rightarrow 2\omega(e)$. The copropagating second harmonic and residual fundamental beams are then passed through a deuterated KDP (dKDP) tripler where the third-harmonic beam is created by type-II phase-matched sum-frequency mixing: $2\omega(o) + 1\omega(e) \rightarrow 3\omega(e)$. We set the critical 2:1 mix ratio of 2ω to 1ω energy needed for efficient mixing in the tripler by angularly biasing the type-I doubler a few hundred microradians from exact phase matching. The optimum bias angle depends both on crystal thickness and drive irradiance. The sensitivity of conversion efficiency to this optimum bias angle is shown in Fig. 20.

Figure 21 shows measured 3ω energy produced as a function of 1ω energy into the converter for FIT pulses. The figure compares two different converter configurations, one with crystal thicknesses $L_1/L_2 = 11\,\text{mm}/9\,\text{mm}$, and a second with $L_1/L_2 = 14\,\text{mm}/10\,\text{mm}$. The data for the 11/9 configuration was obtained from shots with a 3.5 ns pulse length, with the doubler operating at a bias of 220 ± 5 μrad, and with the tripler tuned for phase matching to within ±15 μrad (all angle values are internal to the crystal). At the highest input energy tested (12.9 kJ), this configuration produced an output 3ω energy of

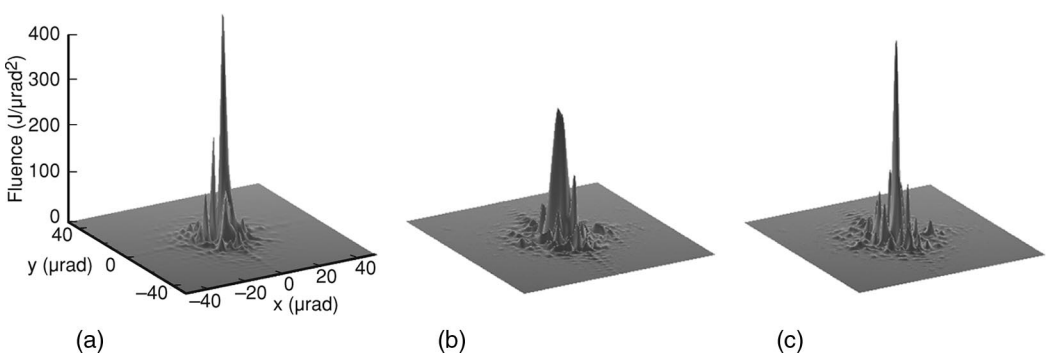

Fig. 18. (a) Calculated and directly measured 1ω focal spots for the (b) first and (c) second PQ shots. All plots have a common axis, which is shown on the left. The change in peak fluence between the first and second shots is attributed to turbulence in the beam path.

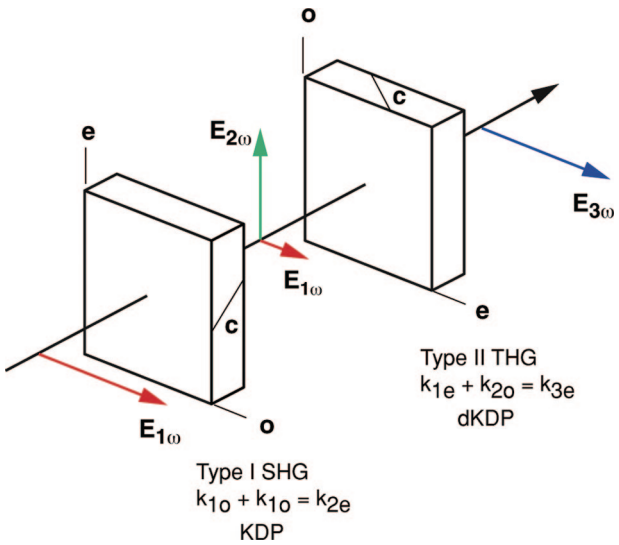

Fig. 19. (Color online) Illustration of type-I/type-II converter scheme. The NIF doubler (SHG) thickness will range from 11 to 14 mm, and tripler (THG) thickness will range from 9 to 10 mm. The measurements described in this paper were primarily performed with a 14 mm SHG and 10 mm THG.

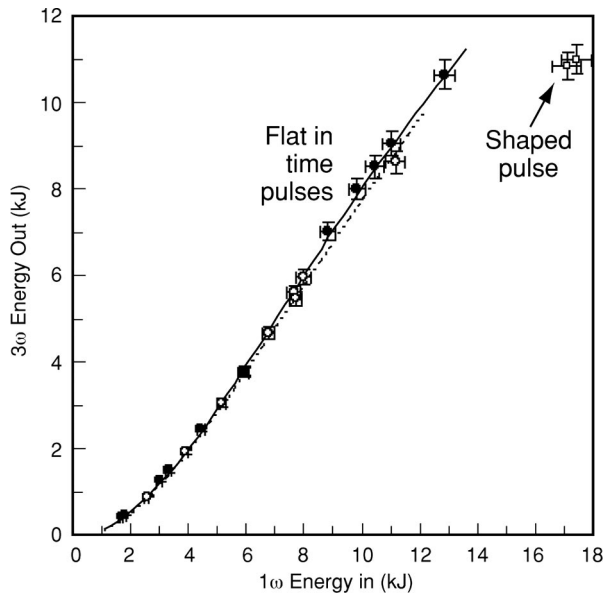

Fig. 21. Measured 3ω energy out of the converter versus measured 1ω energy into the converter for three illustrative cases: an 11/9 converter with 3.5 ns FIT pulses (filled circles), a 14/10 converter with 5.0 ns FIT pulses (open circles). The model (solid curve for FIT 11/9, dashed for FIT 14/10) is described in the text.

10.6 kJ, i.e., the energy conversion efficiency across the converter was >80%. The data for the 14/10 configuration was obtained from shots with a 5 ns pulse length and with the doubler at a bias of 195 μrad. As Fig. 21 indicates, the thicker crystals have better low-irradiance performance than the 11/9 configuration, since a similar conversion efficiency is achieved at approximately two thirds (3.5 ns/5 ns) the drive irradiance. The increased efficiency at low drive is an advantage for converting high-contrast ignition pulses, provided the reduced angular bandwidth of the thicker crystals is manageable (see Fig. 20). Results on the NIF demonstrate that the crystal alignment system is precise enough to allow accurate alignment of the thicker crystals. All 3ω performance data discussed in the remainder of this paper was obtained using the 14/10 configuration.

The measured third-harmonic performance of the laser under PQ conditions is summarized in Figs. 22–24. Figure 22 plots the harmonic energies and pulse

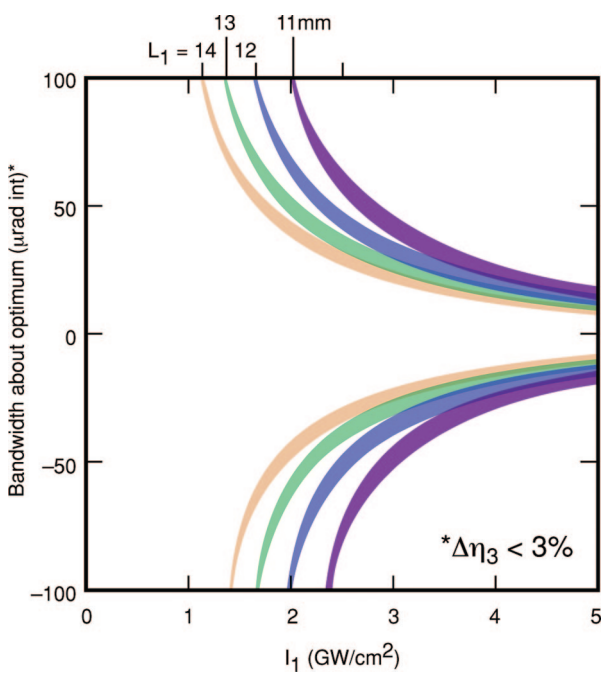

Fig. 20. (Color online) Angular bandwidth of the type-I/type II 3ω conversion scheme versus drive irradiance for different choices of crystal thickness. The curves depict the angle away from exact phase matching at which conversion efficiency is decreased by 3%, with the bands at each SHG thickness (L_1) spanning the THG thickness range from 9 to 10 mm.

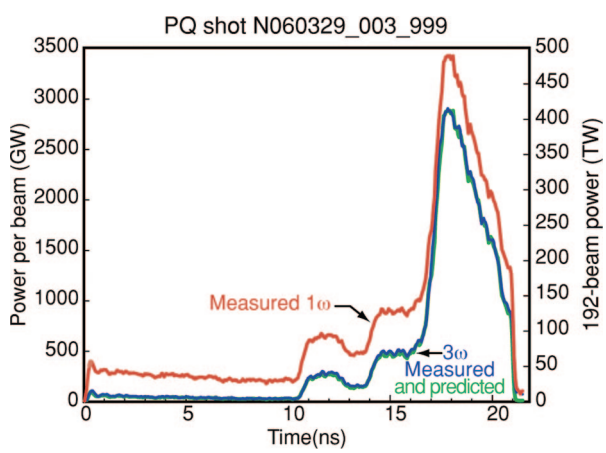

Fig. 22. (Color online) Comparison of measured and predicted pulse shape for the 3ω PQ pulse are shown along with the input 1ω pulse shape.

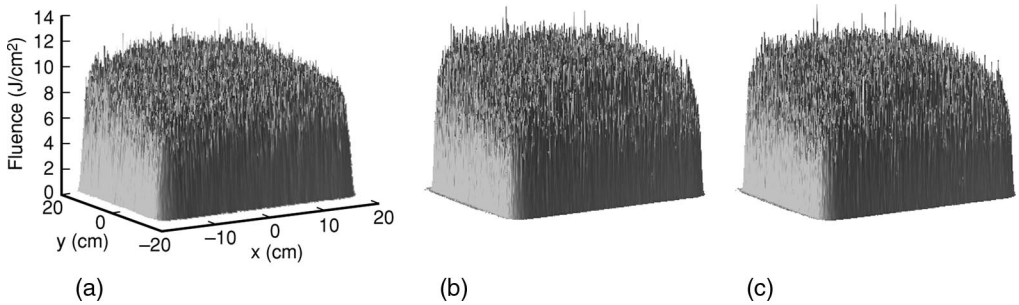

Fig. 23. Comparison of (a) modeled and measured near-field 3ω fluence distributions at PDS for the (b) first and (c) second PQ shots, respectively.

shapes for a 17.1 kJ input pulse with a peak power of 3.65 TW and a temporal contrast of 17:1, frequency converted to 10.9 kJ of 3ω with a peak power of 2.90 TW and a temporal contrast of 150:1 at the output of the converter. The measurements are in good agreement with simulations employing a 3D (x, y, z) time-slice model. The model uses the paraxial formulation of the coupled wave equations and accounts for diffraction, phase matching, Poynting vector walk-off, linear absorption, nonlinear refractive index, cross-phase modulation, and two-photon absorption at the third harmonic [20]. It incorporates representative measured crystal data for surface aberrations [21], spatial birefringence variations [22], as well as measured data for the spatial profile of the electric-field amplitude, phase, temporal waveform of the input pulse (see previous section), and Fresnel losses (Table 3). The first two rows of Table 3 give the Fresnel losses in the converter components [second-harmonic generation (SHG) and third-harmonic generation (THG)]. The final row summarizes the remaining transport losses to the target. The majority of this remaining loss occurs at a grating that is etched onto a silica debris shield, which directs a portion of the light to the drive diagnostic. The simulations were performed on a 512 × 512 transverse spatial grid with 1 mm resolution, using the split-operator method [23,24] and fast Fourier transforms for the field propagation, with 15 z steps per crystal. The temporal pulse shape was modeled with discrete time slices (typically 50). The effect of temporal bandwidth on the input pulse was modeled as an effective tripler detuning of 1.9 μrad/GHz SSD. The model for Fig. 22 uses as field inputs the PDS 1ω measured near-field fluence, radial shear wavefront, and temporal pulse shape. It confirms the ability of the frequency conversion model to match measurements.

LPOM, as discussed in Appendix C and Subsection 3.C, uses the frequency conversion model to predict both energetics and near- and far-field profiles at 3ω. Figure 23 compares the near-field prediction at the output of the final focusing lens with measurements for the two PQ shots. Figure 24 similarly compares the near-field fluence probability distributions over the center 27 cm × 27 cm of the beam. LPOM predicts a beam contrast of 8.7%, slightly lower than the mea-

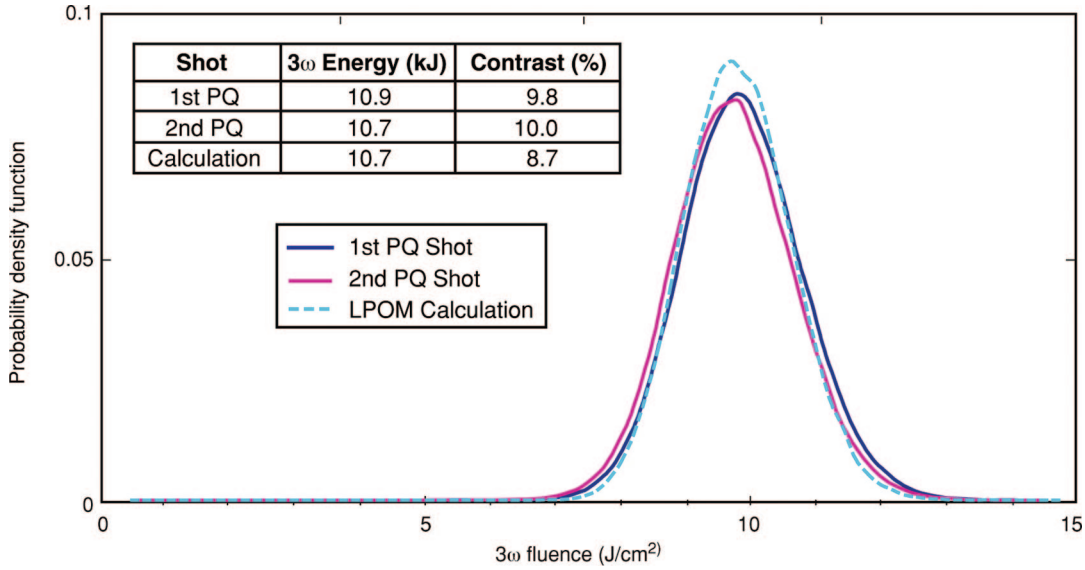

Fig. 24. (Color online) Comparison of modeled and measured fluence probability distributions at 3ω PDS over the central 27 cm × 27 cm of the beam. The calculation is reported at the mean fluence over this aperture for the two shots. Measured contrast is nearly identical for both shots, ~1% higher than the model and well under our design goal of 15%.

Table 3. Transmission of FOA Optics as a Function of Wavelength

Component	Transmission 1ω (1.053 μm)	2ω (0.527 μm)	3ω (0.351 μm)
SHG	0.9900	0.9925	NA
THG	0.9607	0.9766	0.9975
To TCC	0.8995	0.9184	0.9545

sured values of ~10%. As in the 1ω section, the calculation includes an estimate of the contrast added by the 3ω diagnostic optics. The measured value is substantially below the 15% contrast design goal.

Figure 25 shows the enclosed energy fraction of measured and modeled 3ω focal spots as a function of radius, starting at the centroid of the spot. As with the 1ω spots in Fig. 17, two measurements are indicated for each PQ shot: one directly from the PDS far-field camera, the other a reconstruction from the measured near-field fluence and wavefront. The LPOM model agrees reasonably well with the reconstructed-field prediction. Both yield ~10% smaller spots than the far-field camera measurement. Figure 26 shows the LPOM-modeled far field and the directly measured far fields, demonstrating the good qualitative agreement and shot-to-shot repeatability.

4. Focal Spot Beam Conditioning and Precision Pulse Shaping for Ignition Experiments

The PQ demonstrations discussed to this point were shot without focal-spot beam conditioning in order to study the fine-scale characteristics of the NIF focal spots. NIF ignition targets, however, will require spatial and temporal beam conditioning both to tailor the irradiance profile in the focal plane and to reduce hot spots that might seed laser plasma instabilities [12–14] (LPI). Spatial beam conditioning is provided by phase plates designed to produce elliptical speckle patterns with ~1 to 1.3 mm average diameter and ellipticity that varies from beam to beam, depending on the angle of incidence at the target. The contrast of the laser speckle is then reduced, both instantaneously and in a time-averaged sense, by the application of polarization smoothing [25] (PS) and smoothing by spectral dispersion in one dimension [26,27] (1D SSD). Polarization smoothing is limited to a maximum reduction in contrast of $1/\sqrt{2}$ [28]. SSD, as implemented on the NIF, achieves an additional ~5× reduction in speckle contrast on a time scale of a few tens of picoseconds.

The tests described in this section also utilized precisely shaped pulses with high temporal contrast (~150:1), single-beam 3ω peak powers in the range of 1.9–2.6 TW, and energies of 5.2–9.4 kJ (370–500 TW, 1–1.8 MJ full NIF equivalents). The two ignition pulse shapes used in these experiments are shown in Fig. 27. The 1 MJ shape is the current baseline [16] for the first ignition campaign on the NIF. The 1.8 MJ shape is a slightly updated version of the reference ignition pulse shape we assumed for the NIF laser design. For further discussion of pulse-shaping requirements for the ignition point design see Refs. [12–16].

Table 4 summarizes results for two shots: a 1 MJ pulse with a 0.50 mm × 0.95 mm (diameter) elliptical focal spot and 270 GHz of SSD, and a 1.8 MJ pulse with a 1.2 mm × 1.3 mm (diameter) focal spot

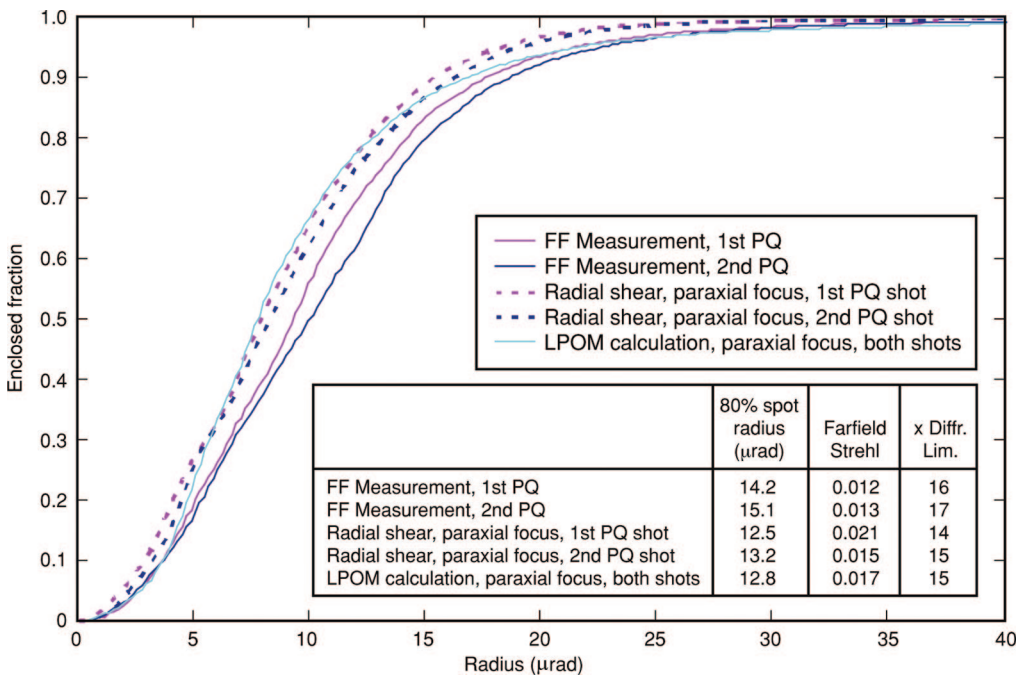

Fig. 25. (Color online) Enclosed 3ω focal-spot energy fractions for measurement and calculation of the two PQ shots. Both direct far-field measurements and predictions based on reconstruction of the field using the radial shear and near-field diagnostics are shown.

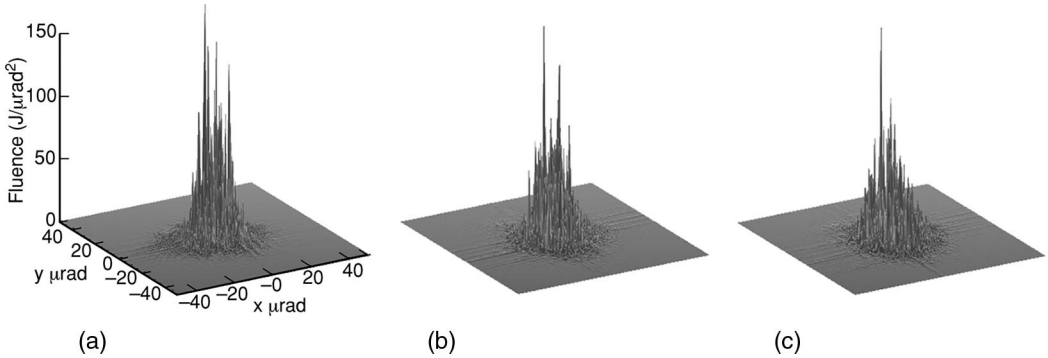

Fig. 26. (a) LPOM-calculated and directly measured 3ω focal spots for the (b) first and (c) second PQ shots. All plots have a common axis that is shown on the left.

and 90 GHz of SSD. (In this section, all SSD bandwidths are specified at 3ω unless otherwise indicated. To good accuracy, the frequency converter triples the imposed bandwidth along with the fundamental laser frequency.) These fully integrated tests included all three of the NIF's beam-conditioning techniques simultaneously: phase plates, smoothing by spectral dispersion, and polarization smoothing. Table 4 shows that the energies, peak powers, focal-spot sizes obtained, and SSD bandwidths for the two candidate ignition temporal pulse shapes agree with expectations and meet or exceed the campaign goals. Polarization smoothing will be accomplished on the NIF by rotating the polarization in two of the four apertures in each final optics assembly by 90°, and then overlapping all four beams at the target. Consistent with this strategy, the tests described here were conducted with a prototype dKDP 1ω half-wave plate and a rotated set of frequency conversion crystals installed in the PDS final optics (Fig. 28). The average polarization impurity of a low-power pulsed 1ω beam (generated by leaving the rod and slab amplifiers unpumped) was measured both with and without the wave plate (Fig. 29) and found to be better than 0.11% in each case. This level of depolarization has a negligible impact on frequency conversion. Phase-plate divergence and SSD bandwidth do affect frequency conversion and must be taken into account. These effects are addressed below in the discussion on pulse shaping.

A. Spatial Beam Conditioning with Phase Plates

Phase plates (kinoforms) enlarge and shape the focal spot by introducing phase aberrations on the beam in a controlled manner. Early implementations employed binary random phase plates [29] (RPPs) and multilevel discontinuous kinoform phase plates [30] (KPPs). The NIF will employ continuous phase plates (CPPs), which have smooth phase profiles with no abrupt discontinuities that can adversely affect the beam near-field characteristics [31,32]. The phase profiles for these plates are designed using a modified Gerschberg–Saxton algorithm [31], and they are imprinted onto 430 mm × 430 mm × 10 mm fused-silica plates using a magnetorheological finishing (MRF) process [33]. These CPPs are achromatic, affording flexibility in their placement relative to the frequency conversion crystals. For the tests described here, the plates were solgel antireflection coated for 1ω operation (<0.2% Fresnel loss per surface) and installed in the PDS final optics as shown in Fig. 28.

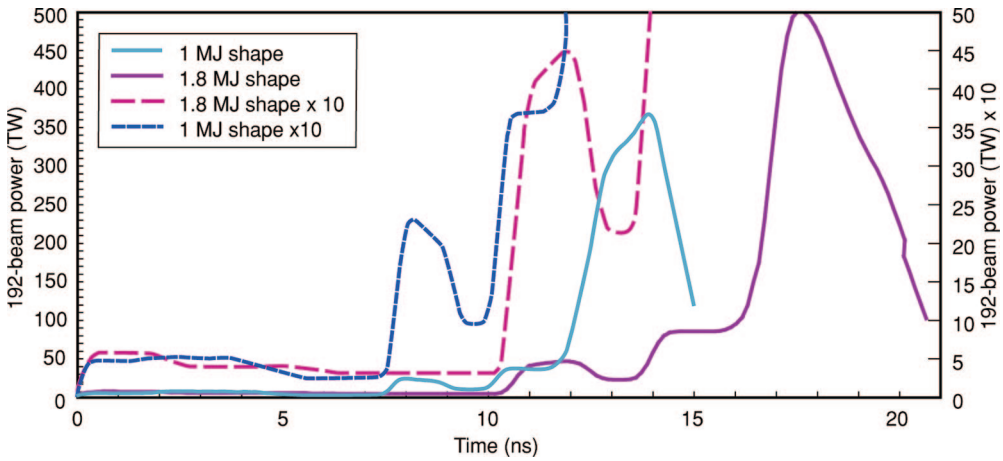

Fig. 27. (Color online) The two shaped pulses that were used in these experiments, scaled to their 192 beam equivalents. The temporal contrasts are 158:1 and 176:1 for the 1 and 1.8 MJ pulses, respectively.

Table 4. Three Methods of Beam Conditioning Were Demonstrated Simultaneously on Two Candidate Ignition Temporal Pulse Shapes

Campaign Description			Beam Energy and Power			Beam Smoothing		
Campaign	Pulse Shape	Pulse Length (ns)	3ω Energy per Beam (J)	3ω Energy Full NIF (MJ)	Peak Power (TW/Beam)	CPP (mm) [FWHM]	Polarization Rotation	SSD (GHz 3ω)
1.0 MJ ignition design	Ignition	15.4	5208	1.00	1.85	0.95 × 0.5	Yes	270
Demonstrated: 1.0 MJ	Ignition	15.4	5316	1.02	1.9	0.95 × 0.5	Yes	270
1.8 MJ ignition design	Ignition	20.4	9375	1.80	2.6	1.3 × 1.16	Yes	90
Demonstrated: 1.8 MJ	Ignition	20.4	9438	1.81	2.6	1.3 × 1.16	Yes	120

Figure 30 compares measured and modeled focal spots obtained with the appropriate CPPs for the 1.0 and 1.8 MJ pulses with no SSD present. We also compare (Fig. 31) the encircled energy for these spots and the fractional power above intensity (FOPAI), defined as

$$\mathrm{FOPAI}(I_0) = \frac{\displaystyle\int_{\substack{\text{beam area}\\ \text{where } I(x,y)\geq I_0}} I(x,\ y)\mathrm{d}x\mathrm{d}y}{\displaystyle\int_{\text{beam area}} I(x,\ y)\mathrm{d}x\mathrm{d}y}. \qquad (2)$$

The model starts with the measured 1ω near-field fluence, temporal shape, and phase profiles (from the PDS radial shear interferometer), then adds the measured CPP phase to construct the complex 1ω electric field. It then calculates the frequency conversion of this beam and the propagation of the resulting 3ω beam through the final optics and to focus. The modeled FOPAI is evaluated at the time of peak power. We derive the measured FOPAI by assuming that the intensity is separable in time and space: $I(x, y, t) = F(x, y) * P(t)/E$, where F is the measured near-field fluence, P is the time-dependent whole-beam power, and E is the total energy. Equation (2) is, again, evaluated at the time of peak power. Our models indicate that, for these pulses, intensity-dependent effects such as nonlinear refractive index and frequency conversion, do not cause significant changes in the focal-spot characteristics as a function of time, justifying the separability assumption above. Figures 30 and 31 show that the modeled and measured focal spots are in good agreement. The encircled energies and the FOPAI also agree well for both the 1 MJ and the 1.8 MJ CPP spots.

The smallest speckle size in the patterns seen in Fig. 30 is $2\lambda f/D = 15.4\ \mu\mathrm{m}$, the diffraction limit of the final focusing lens. Although the contrast of an ideal speckle pattern is unity, the measured focal spots show a lower contrast of 0.79 ± 0.02. We account for this nonunity value by noting the presence of the SBS-suppression bandwidth (3 GHz FM modulation, 30 GHz FWHM at 1ω, 90 GHz at 3ω) and the chromatic dispersion in the wedged final focusing lens. The lateral displacement in the focal plane due

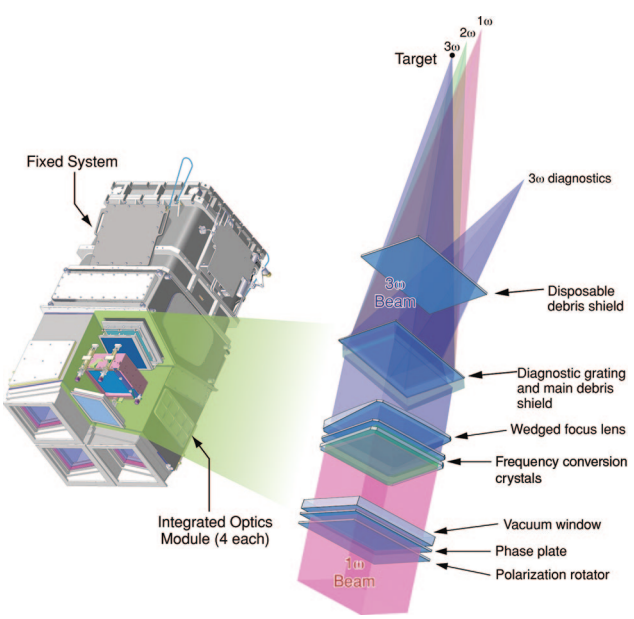

Fig. 28. (Color online) Schematic layout of the final optics assembly on the NIF is shown on the left. This mechanical system mounts to the NIF target chamber and contains the final set of optics for four NIF beamlines. The suite of optics for one of these beamlines is shown on the right. The same mechanical, optical, and beam control components that are used in the FOA at the target chamber are reproduced for a single beamline in the PDS.

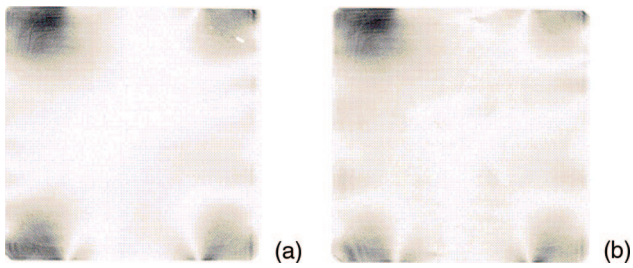

Fig. 29. (Color online) Measured depolarization on the NIF beam (a) without and (b) with the polarization rotator crystal. The linear gray scale varies from 0% (white) to 2% (black) depolarization. The spatial extent of the image is 38 cm on each side. The small spatial variations of beam polarization are due to the stress-induced birefringence in the vacuum-loaded spatial filter lenses. The average depolarization is 0.11% for each case, which results in a frequency conversion loss that is both small compared to the 1ω and 3ω FOA transmission losses shown previously in Table 3 and negligible in an absolute sense.

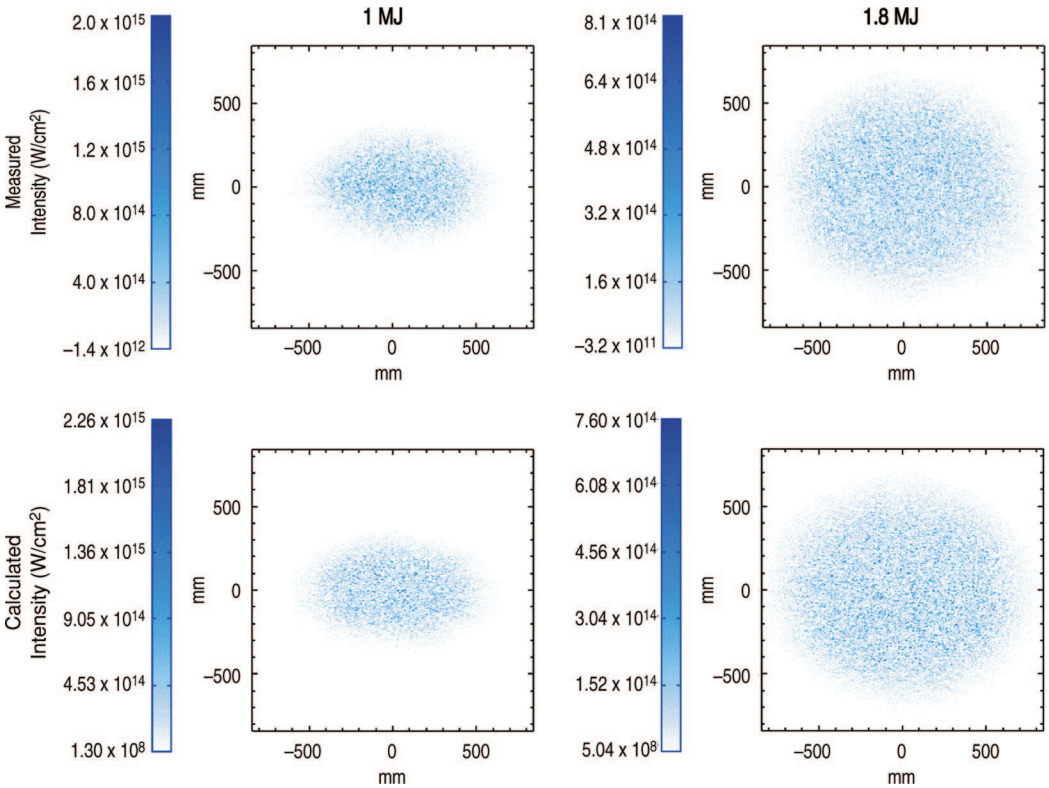

Fig. 30. (Color online) Comparison of measured (top) and calculated (bottom) NIF focal spots with no applied SSD. The images on the left are from a 1 MJ shot with a 0.50 mm × 0.95 mm FWHM spot-size CPP. Images on the right are from a 1.8 MJ shot with a 1.16 mm × 1.3 mm FWHM spot-size CPP. The measured data are from the shots described in Table 4. Measured (time-integrated) images and calculated (time-dependent) images are both normalized to an input power of 1 TW. See text for discussion.

to the lens chromatic dispersion is ~0.045 μm per GHz at the third harmonic. When averaged over the pulse length, the shifted speckle patterns add incoherently and reduce the contrast, in a process analogous to SSD. This effect predicts a decrease in contrast to 0.84, in reasonably good agreement with the measurement.

B. Temporal Beam Conditioning with One-Dimensional Smoothing by Spectral Dispersion

SSD consists of phase modulating the laser pulse and angularly dispersing its spectral content sufficiently to displace individual FM sidebands in the focal plane by at least half the speckle size, a condition generally referred to as "critical dispersion" [26,27]. On the NIF, the SSD modulator runs at 17 GHz (ν_{mod}), and the 3ω lateral spectral displacement at the target is 0.58 μm/GHz—comfortably beyond the critical dispersion value of 0.45 μm/GHz. This dispersion is provided by a Littrow grating, in the preamplifier module oriented so that the dispersion direction is aligned along the short axis of the elliptical focal spot. SSD bandwidths of up to ~150 GHz (1ω) can be produced by adjusting the modulation index (δ) of the

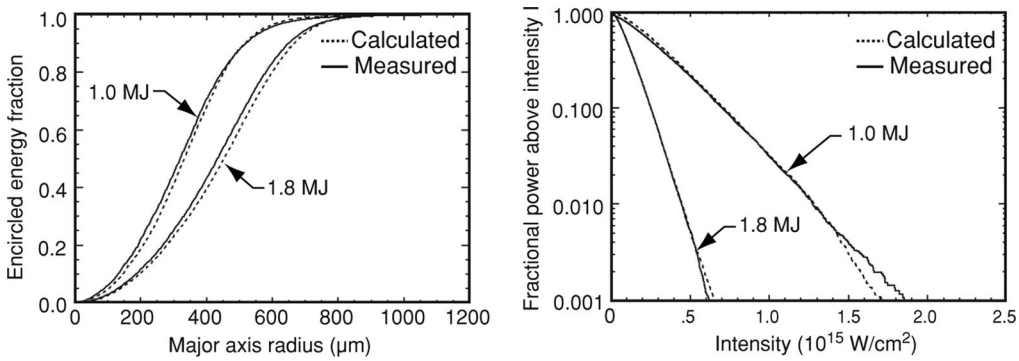

Fig. 31. Comparison of the encircled energy fraction and the FOPAI for the 1 MJ and the 1.8 MJ shots described in Fig. 30. The encircled energy was calculated in elliptical coordinates with eccentricity of 0.55 for the 1 MJ case and 0.88 for the 1.8 MJ case. The total power is normalized to 1 TW for each case.

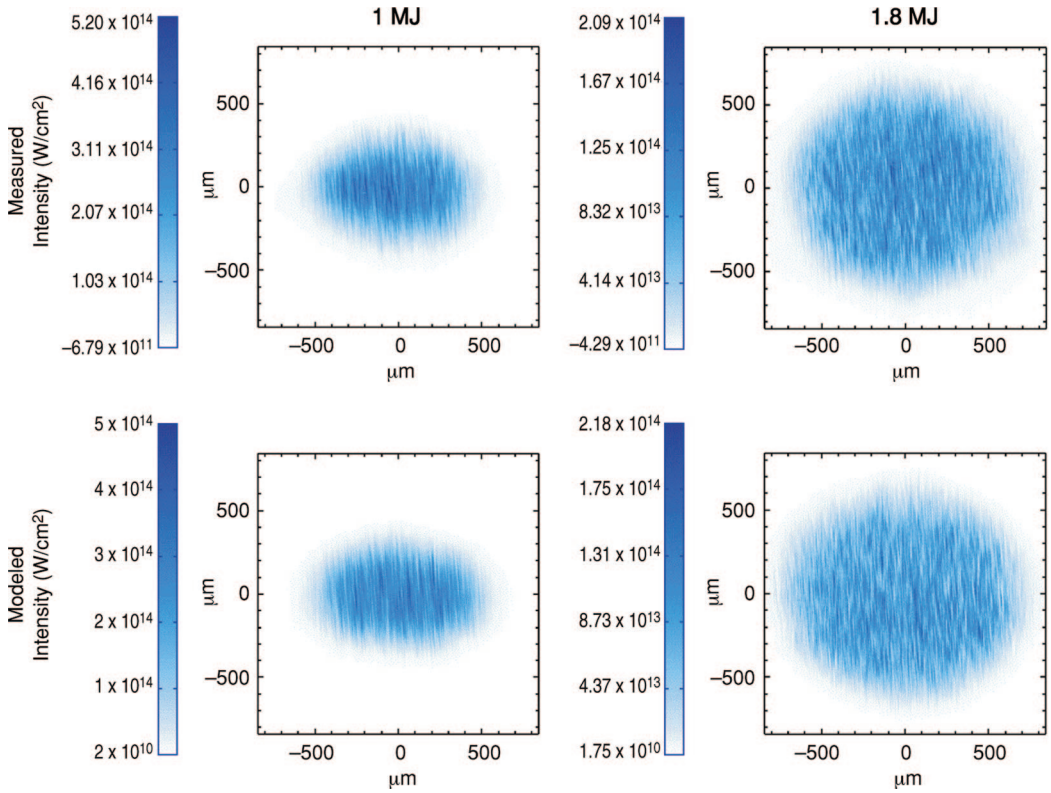

Fig. 32. (Color online) Comparison of measured (top) and calculated (bottom) focal spots with both CPP and SSD. The images on the left are from a 1 MJ shot with a 0.50 mm × 0.95 mm FWHM spot size CPP. The images on the right are from a 1.8 MJ shot with a 1.16 mm × 1.3 mm FWHM spot-size CPP. The measured data are from the shots described in Table 4. The 3ω spectra used to generate the predictions are shown in Fig. 33. The spots are normalized for 1 TW total power.

modulator ($\Delta\nu_{1\omega} = 2\delta\nu_{\mathrm{mod}}$). The maximum 1ω bandwidth in the tests reported here was measured to be 95 ± 5 GHz.

Figure 32 compares the measured and calculated focal spots with both CPP and SSD for the 1 MJ PQ shot and for one of the 1.8 MJ ignition pulses. The time-averaged SSD focal spot was calculated by performing a spectrally weighted incoherent sum of spatially translated non-SSD focal spots (Fig. 30), using the measured 3ω spectrum (Fig. 33). This spectrum includes both the 3 GHz modulated SBS-suppression bandwidth and the 17 GHz modulated SSD bandwidth. The calculations include both the lens chromatic dispersion (horizontal in the figure) and the grating SSD dispersion (vertical). The observed reduction in speckle contrast from 0.79 to 0.19 for the 1 MJ focal spot is equivalent to an incoherent average of ~28 speckles. The speckle contrast for the 1.8 MJ spot decreased from 0.79 to 0.24, which compares well with the calculated decrease to 0.26 and corre-

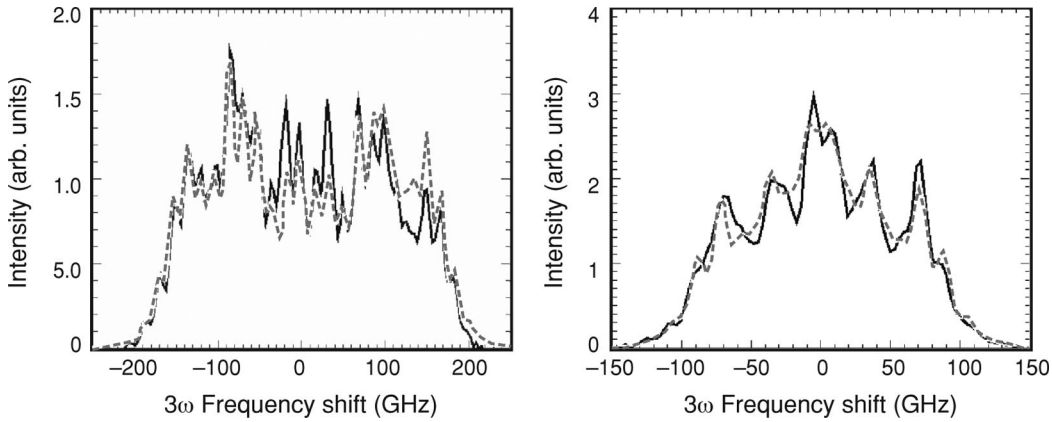

Fig. 33. Measured (solid curves) and the fitted (dashed curves) spectra for the 1 MJ (left) and the 1.8 MJ (right) shots described in Table 4. The fit assumes a sum of 3 and 17 GHz FM components and yields 3ω SBS bandwidths of 90 GHz for both cases and 3ω SSD bandwidths of 270 and 120 GHz for the 1 and 1.8 MJ shots, respectively.

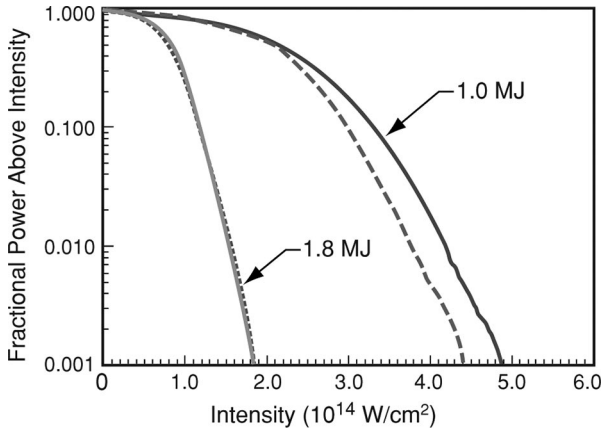

Fig. 34. FOPAI comparisons for CPP-generated, SSD-smoothed focal spots. All curves are normalized to 1 TW total power. Solid curves are measurements; dashed curves are model. The 1 MJ curves are on the right; 1.8 MJ on the left.

sponds to averaging of ~16 speckles. The effect of speckle averaging can be seen by comparing the images of Fig. 30 (no SSD) with those of Fig. 32 (with SSD). FOPAI plots for both the 1 MJ and the 1.8 MJ focal spots (Fig. 34) demonstrate both the reduction of the intensity of the hot spots by SSD and the agreement between prediction and measurement of that decrease.

C. Frequency Conversion of Spatially and Temporally Conditioned Pulses

Precision pulse shaping requires an accurate laser energetics model that, among other things, correctly accounts for conversion efficiency losses associated with beam conditioning. Table 5 summarizes the results of a series of high-power shots conducted with 1 ns, flat-in-time pulses for the purposes of validating our converter model. Data were obtained at a drive irradiance of ~3 GW/cm^2 for three different 1ω CPP configurations (none, 0.50 μm × 0.95 μm, and 1.16 μm × 1.3 μm), each with varying amounts of SSD bandwidth. The two CPP spot sizes correspond to the point designs for the 1 and 1.8 MJ ignition experiments, respectively. The relevant energies are shown at the input to the SHG (1ω at input to SHG) and the output of the THG (3ω at THG output). For each shot, conversion efficiency was calculated using the model described in Section 3, including measured phase profiles for the phase plates. Bandwidth was simulated as an effective tripler detuning of 1.9 μrad/GHz (1ω), assuming quadrature addition of the 3 and 17 GHz spectra. Off-line time-dependent plane-wave calculations have validated that bandwidth can be treated as an effective detuning over a wide range of power. In all cases, the model is within 2.5% of measurement.

D. Temporal Pulse Shaping

The ignition campaign plan calls for a high-contrast, frequency-tripled temporal pulse shape, with all beam-conditioning techniques in place, to be specified and controlled to a root-mean-square deviation over the 48 NIF quads of ≤15% in the foot of the pulse and to ≤3% at the peak of the pulse. A precision pulse-shaping sequence was performed to test how well the current NIF hardware can generate the requested pulses, and to develop a strategy for routinely matching them with high accuracy. Figure 27 shows the requested pulse shapes for the current 1 and the 1.8 MJ baseline target drives.

The LPOM code is the first and primary tool used to determine the required setup pulse shape at the MOR. It uses its calibrated model of the state of all individual components, along with a solver capability built into its propagation and/or extraction code (VBL) to perform a first-principles numerical solution. As a side benefit of this solution, the LPOM predicts the expected pulse shape that will be measured at the ISP and the OSP. For flat-in-time pulse shapes, we have found this solution to be very accurate. For precise control of high amplitude contrast pulses, we have developed an iterative operational procedure to refine the LPOM's results and adjust for minor discrepancies between the model and measurements.

As Fig. 35 demonstrates, this iterative procedure led to an accurate match between the requested pulse shapes at both 1 and 1.8 MJ. Once minor corrections to the drive prescription have been derived, the results can be incorporated into the general LPOM de-

Table 5. Comparison between Modeled and Measured Frequency-Converter Performance

Shot	CPP (MJ)	SSD (1ω GHz)	SHG Input (kJ)	THG Output (kJ) Measured	THG Output (kJ) Model	Delta (%)
N060214-002	—	0	3.759	2.920	2.9072	−0.44
N060216-003	—	65.8	3.644	2.668	2.7122	1.66
N060216-002	—	95.2	3.721	2.477	2.4540	−0.52
N060224-001	1	0	3.672	2.925	2.9325	0.26
N060224-002	1	96.7	3.668	2.462	2.4551	−0.28
N060313-001	1.8	0	3.553	2.656	2.7120	2.11
N060314-002	1.8	37.2	3.757	2.667	2.7336	2.50
N060314-001	1.8	94.8	3.766	2.367	2.3871	0.85

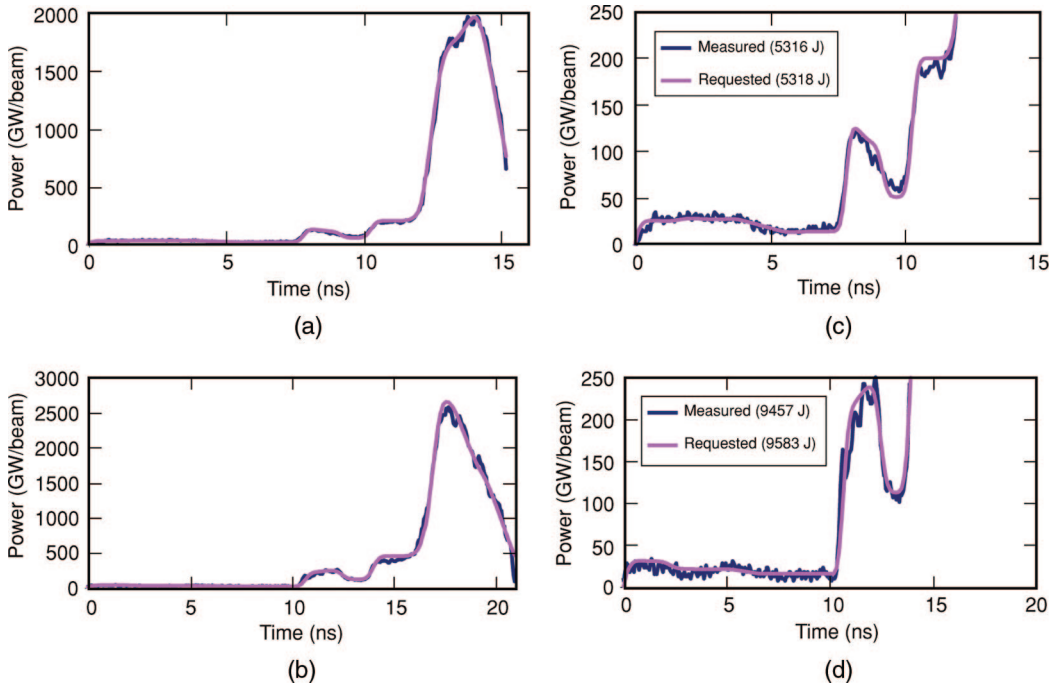

Fig. 35. (Color online) Comparison of measurement to request for 1 MJ [(a) and (b)] and 1.8 MJ [(c) and (d)] pulses, showing the peak [(a), (c)] and foot [(b), (d)] for both.

scription. The LPOM can then be relied on to make the desired pulse modifications required for optimizing the drive to ignition capsules.

5. Summary

The first eight of 192 laser beams in the NIF laser have been tested extensively. These tests generally indicate that the laser meets or exceeds all of its design goals. Flat-in-time and shaped pulses have been fired spanning a wide range of operating conditions. These initial 3ω shots, combined with the validation of our LPOM projections, indicate that the NIF is capable of operating throughout the entire design envelope described in 1994 [7]. Two complex ignition-target temporal pulse shapes were generated on one beamline, with full-scale phase plates, polarization smoothing, smoothing by spectral dispersion, and frequency conversion simultaneously present. Elliptical, flat-top focal-spot profiles, in agreement with predictions, were formed.

These tests also demonstrated the ability of the LPOM to accurately predict laser and frequency-conversion performance and to set up complicated pulse shapes in a relatively short period of time. The NIF design requirement of being able to fire at shot intervals of not more than 8 h was tested by shooting full system shots separated by 3 h and 18 min. No degradation was observed in the beam wavefront, the 1ω or 3ω focal spot sizes, the near-field contrasts, or the temporal pulse shapes.

Commissioning of the remaining bundles of the NIF laser is proceeding and accelerating. We look forward to full-scale target shots beginning in early 2009.

Appendix A: Precision Diagnostic System

In addition to the ISP and output sensor package (OSP) that are integrated into each beamline, the NIF has available a separate PDS containing an extensive suite of diagnostics that can be used for detailed performance characterization of one selected beamline of the NIF laser as illustrated in Fig. 36. PDS is located between Laser Bay 2 and the target chamber in switchyard 2. Mirrors in the roving mirror diagnostic assembly (RMDA) can be positioned to redirect any one of the eight beams from Bundle 31 to the PDS prior to its entry into the target bay. The selected beam is steered by mirrors PM1 through PM6 to the partially reflecting mirror PM7, where 4% of the energy continues to the 1ω diagnostics area while the other 96% is reflected and sent to the 3ω diagnostic section. In the 3ω PDS FOA, the 1ω beam is converted to the third harmonic and brought to focus in the middle of the prime focus vessel (PFV). Downstream of the PFV, a 1 m aperture, three mirror telescope housed in the vacuum environment of the target diagnostic chamber (TDC) is used to image the 3ω focal plane inside the PFV onto diagnostics on optical tables arrayed around the TDC.

The PDS was used extensively to test frequency-conversion performance of the FOA. For this purpose, accurate measurements of the FOA input and output beam energies are essential. At the PDS, a total of six calorimeters are used for this purpose. The locations of these calorimeters are indicated in Fig. 36. They include the whole-beam (WB) calorimeter and the 1ω calorimeter on table T03 that are used to monitor the 1ω energy incident on the FOA,

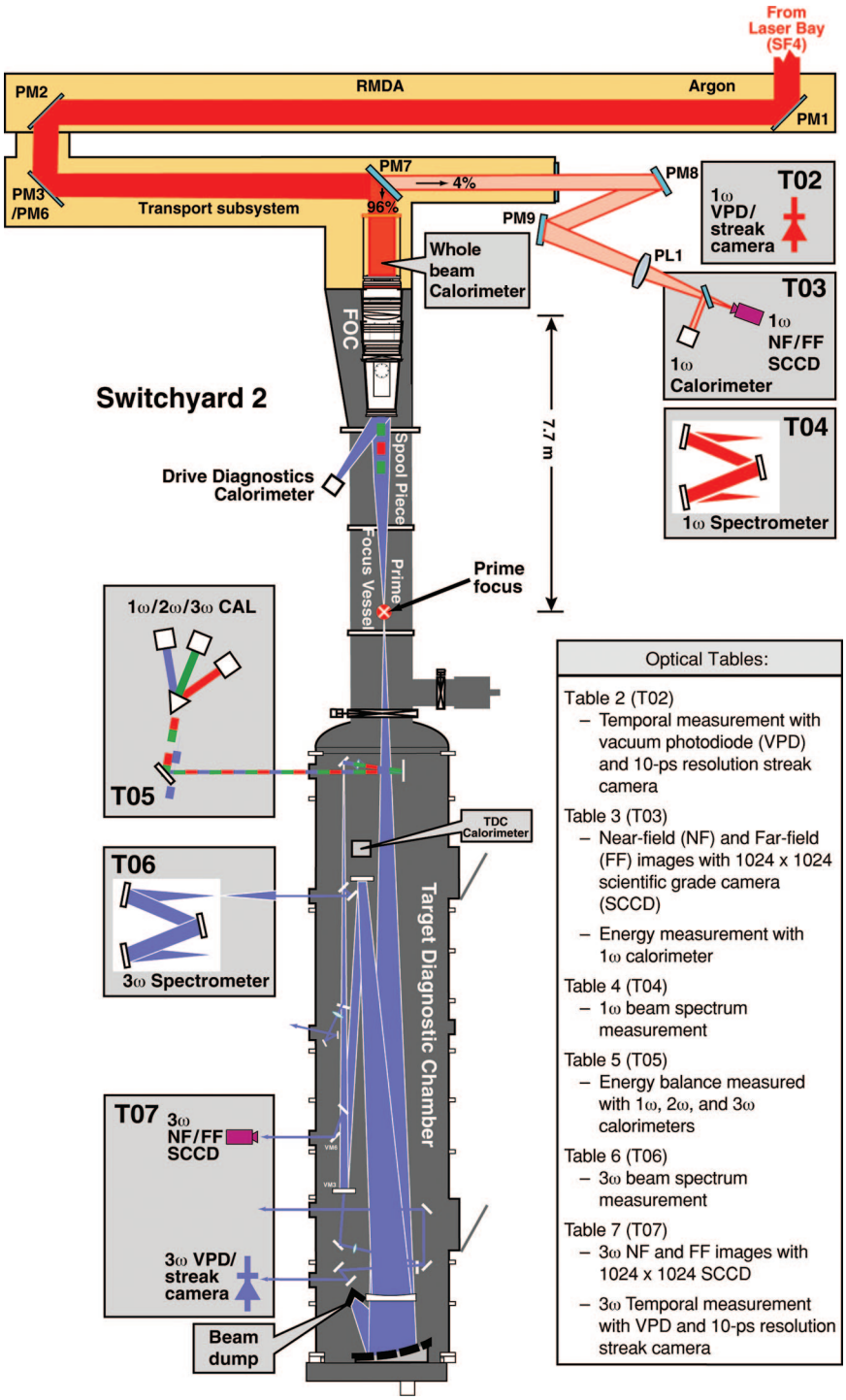

Fig. 36. (Color online) PDS layout showing the optical path and locations of the diagnostics.

the drive diagnostic (DrD) calorimeter that measures the generated 3ω energy, the TDC calorimeter, that measures the sum of the 1ω, 2ω, and 3ω energies after the converter, and the three calorimeters on table T05, which measure 1ω, 2ω, and 3ω energies individually after they are separated by prisms. Because of the different energy ranges and beam formats of the various color beams, the aperture sizes of these calorimeters range from 2.54 cm diameter to as large as 44 cm × 44 cm. PDS calorimeters are calibrated to within ±1% relative to NIST standards in an off-line facility. Energy measurements inferred from these calorimeters include small uncertainties in transport optics efficiencies. Comparison among the various energy diagnostics (DrD, TDC, T05 calorimeters) and estimates of the additional uncertainties both indicate absolute 3ω energy accuracy of ±2% relative to the original NIST standards. An ex-

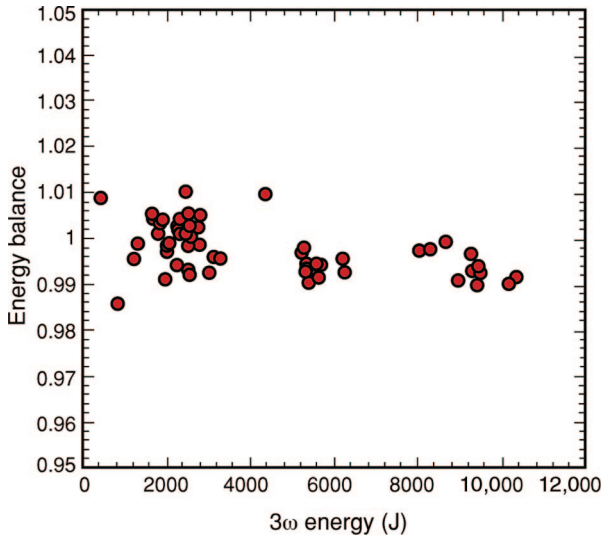

Fig. 37. (Color online) Calorimeter energy balance for shots fired during the PDS campaign plotted against the 3ω energy generated.

ample of this comparison among diagnostics is the verification of energy balance: the comparison of the input 1ω energy to the sum of the 1ω, 2ω, and 3ω energies after conversion with allowance for the known losses in the converter. Figure 37 shows the energy balance for the 67 shots reported in this paper. Aside from one shot at low energy, energy balance is maintained to within ±1%, consistent with the quoted calorimeter accuracy.

The PDS is also uniquely equipped to perform detailed characterization of the NIF laser beam spatial profiles. For this purpose, it contains several large-aperture imaging optics and scientific-grade charge-coupled-device (CCD) cameras.

In the 1ω diagnostic area, the full-aperture beam is first reduced in size using a 61 cm diameter aspheric lens (PL1), then is captured by a near-field camera, a far-field camera, and a wavefront sensor. The high-resolution near-field image provides measurement of beam contrast and allows detection of any high-fluence hot spots. The wavefront data, measured with radial shear and Hartmann sensors, assesses the effectiveness of wavefront correction by deformable mirrors in the main beamline.

In the 3ω diagnostic section, a 1 m aperture, three mirror telescope housed in a 2.2 m diameter × 12 m long vacuum tank image relays the FOA plane and the 3ω focal region at the prime focus onto 3ω high-resolution CCD cameras. The near-field image of the FOA output plane detects hot spots and diagnoses conversion performance across the beam aperture. The 3ω focal region in the PFV is equivalent to the location of the NIF target chamber center. We image this in the far-field CCD to characterize the irradiance profile on the NIF targets.

To check the overall imaging performance of the 3ω far-field optics, we image a 3ω point source located at the prime focus. The result is shown in Fig. 38. The imaged spot fits well to a classic Airy pattern, with a central lobe diameter of 18 μm between the first nulls. Since the telescope f number is 20, the measured beam diameter is 1.1 times the diffraction limit. This near-diffraction-limited performance and the high magnification (10.5×) of the 3ω far-field camera setup mean that 7.3 μm beam speckles, resulting from the use of phase plates for beam smoothing, are well resolved.

The NIF laser beam is frequency modulated both to achieve beam smoothing by spectral dispersion and to suppress stimulated Brillouin scattering in the high-fluence optics. We used a pair of 1 m $f/5.8$ McPherson model 2051 imaging spectrometers to monitor the frequency spectrum and to determine the absolute wavelength of the NIF laser at 1ω and 3ω. The 1ω and 3ω spectrometers were calibrated to an accuracy of ±0.02 nm by measuring spectral lines from a Ne calibration lamp. As seen in Fig. 39, we measured a FWHM linewidth of 8.4 GHz for the Ne

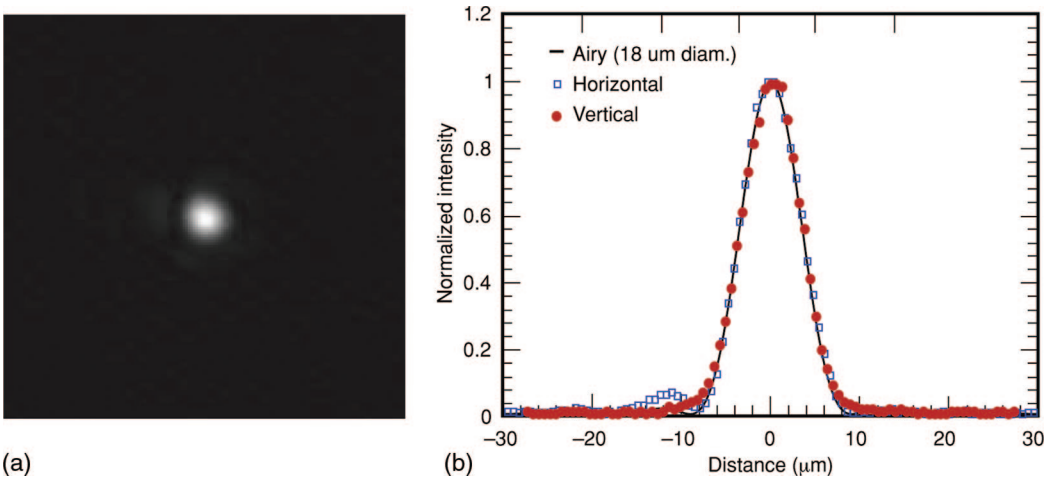

Fig. 38. (Color online) Measurement and model of 3ω point source located at the prime focus. (a) CCD image cropped to a size of 100 μm × 100 μm at the image plane, (b) horizontal and vertical line-outs superimposed on an Airy diffraction pattern model with a central lobe diameter of 18 μm between the first nulls.

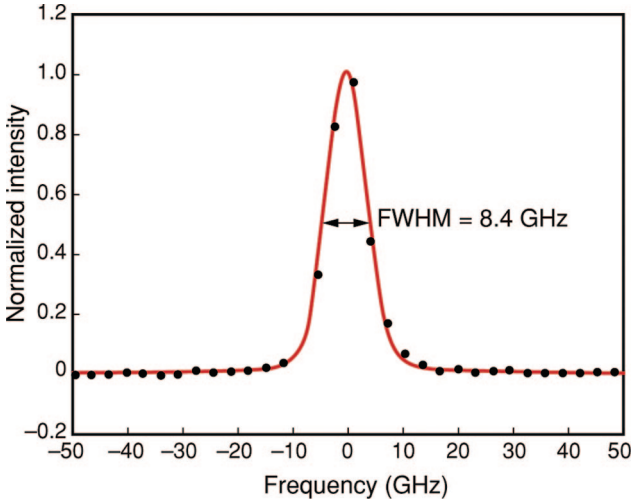

Fig. 39. (Color online) Measured Ne spectral line at 352.04714 nm using the PDS 3ω spectrometer. The line shape is a convolution of the Ne line with the spectrometer instrument response function, implying an instrumental FWHM of ~5.7 GHz.

line at 352.047 nm. Deconvolving the intrinsic width of the neon line, we infer an instrumental response of 5.7 GHz FWHM.

Fusion ignition experiments call for a precisely shaped temporal pulse. The PDS detects 1ω and 3ω pulse shapes with high-speed Hamamatsu R1328U series vacuum photodiodes (VPD), coupled to a 6 GHz Tektronix TDS6604 scope. The detector and scope combination has a 10% to 90% rise time of 98 ps and a 6 dB electrical bandwidth of 5.2 GHz. The effective dynamic range of the power sensor system for measurement of pulses with high-power contrast is increased by splitting the signal from the VPD evenly into two channels of the digitizers with different sensitivity settings. We then stitch the detected pulses from the two channels back together to form the complete pulse. The resulting dynamic range is 1000:1. LLNL-made streak cameras with temporal resolution of 10 ps are also available for detecting high-frequency temporal structure. They have been used to quantify a 17 GHz amplitude modulation resulting from the SSD modulator.

Operation of the PDS diagnostics is controlled by the NIF's integrated computer control system (ICCS). The PDS operator manages all PDS diagnostics remotely from the control room using a graphical user interface, which contains a layout of PDS with each diagnostic represented by individual icons. Clicking on an icon brings up the control panels associated with that diagnostic. During shot time, initial setup, status checking, shot capture, and postshot data archiving, the various diagnostics are coordinated automatically according to programmed scripts. Immediately after the shot, analysis of the data from PDS diagnostics is performed automatically and presented in a shot report. This rapid analysis is an important part of the NIF's capability to operate with short intervals between system shots.

In summary, the PDS fills a unique and critical role in the NIF commissioning. As reported in this paper, it has been used to verify the end-to-end performance of one beamline of the NIF's first bundle.

Appendix B: Laser Diagnostics

The ISP and OSP, present on all the NIF beamlines, are the primary 1ω diagnostic packages on the NIF. These two packages are shown schematically in Fig. 40. The ISP characterizes the beam emerging from the PAM before the four-way split in the preamplifier beam transport system (PABTS). The OSP characterizes each beamline immediately after the transport spatial filter (TSF).

From Fig. 40, one can see that a sample of the beam from the PAM passes through a partially transmissive mirror to a diagnostic path containing an integrating sphere with a diode, a video camera, and a fiber launcher that connects via fiber links to a power sensor and a streak camera. Both the video camera and the power sensor and/or streak camera have variable wedged attenuators to adjust the signal level and avoid saturation.

The integrating sphere diode measures the energy from the PAM. The diode signal is processed by a gated integrator and the result is stored in the NIF database. A flip-in mirror can direct the entire beam to a calorimeter (see Fig. 40), allowing calibration of the diode. The calorimeter is portable and is moved from ISP to ISP to calibrate all of the diodes. For normal operation, the flip-in mirror is removed.

The video camera is a Basler model A102F with a 1392 pixel × 1040 pixel array and 12 bit luminosity resolution. The camera's primary mission is to capture near-field images. To maintain flexibility, however, the lens system in front of it has been designed to also allow far-field operation.

The fiber launcher collects light into a large core multimode fiber and transports it to both a streak camera and a power sensor. For the shots conducted in this test, the streak camera was moved to PDS (See Appendix A). The power sensor consists of a Hamamatsu 1328U-51 vacuum photodiode connected to a fast scope and a Tektronix TDS6604 digitizer. Each sensor handles several beams. The beams are delayed with respect to each other in fiber and are digitized sequentially. The diagnostic package has a bandwidth of ~6 GHz.

The quad backreflection sensor shown in Fig. 40 is used to measure the energy of any backreflected light directed toward the PAM.

The OSP along with the relay optics (RO) diodes and roving calorimeters are used to characterize the beam once it has passed through the main laser. As shown in Fig. 40, a diagnostic beam splitter just downstream from the TSF reflects ~0.1% of the light back into the TSF, where a set of relay optics directs it to the OSP. Before the OSP, a small portion of the light is diverted to a set of diodes, each of which is located inside an integrating sphere. We call these detectors at this location, RO diodes, although the integrating sphere and/or diode packages are identi-

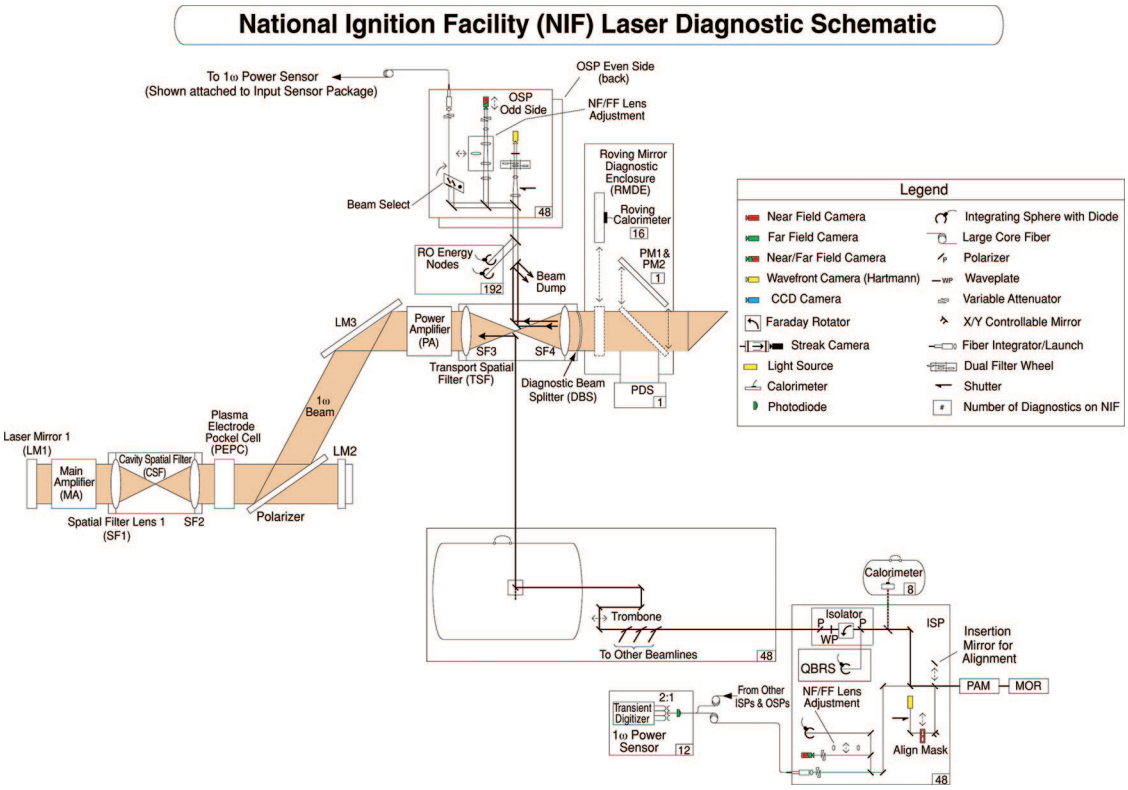

Fig. 40. (Color online) Schematic of the ISP (bottom) and OSP (top) 1ω diagnostics. Light is directed to the OSP from the diagnostic beam splitter.

cal to the ones used in the ISP. There is one such detector for each beam, and it is used to measure total beam energy. We calibrate the RO diodes by inserting a calorimeter in the beam path to establish an energy reference. There are eight roving calorimeters allowing the calibration of all eight beams in a single bundle at the same time. As the name implies, the roving calorimeters can be moved from bundle to bundle to calibrate all of the RO diodes in the NIF. For target chamber shots, the roving calorimeters are removed from the beam path and the RO diodes measure the 1ω energy in each beamline.

Each bundle has four OSP packages, top left, bottom left, top right, and bottom right. Each OSP package, which can accommodate two beams, consists of a video camera, a Hartman sensor and a fiber launcher leading to a remotely located streak camera (not used in this series of tests), and a power sensor. Variable wedged attenuators in front of the camera and fiber launcher control signal sensitivity and saturation.

The OSP camera is identical to that in the ISP and images two beams simultaneously. The two beams on the CCD chip are sized so that each beam is roughly 350 pixels × 350 pixels, allowing for ~1 mm spatial resolution for all near-field images. The optics package in front of the camera (see Fig. 40) allows several different modes of operation including near field and far field.

The remotely located power sensor is the same as for the one in the ISP, with the same 6 GHz response. For the OSP, the power sensor accommodates only one beam, so power waveforms can be measured on half of the beams in each shot.

The OSP Hartman sensor uses the same Basler camera described above with two side-by-side lenslet arrays attached to the front. Each array contains 77 lenslets and allows the capture of wavefront information for both beams diagnosed by the OSP. A fast filter wheel in front of the Hartman sensor allows filters of fixed neutral density to be rotated in front of the Hartman sensor to avoid signal saturation. Filtering in front of the Hartman sensor must change by several orders of magnitude before the main laser is fired. Activation time for the wheel, however, is much shorter than that for the ISP wedged filters, so we can monitor the wavefront of an alignment beam up until 1 s before firing of the main laser.

Appendix C: LPOM

For its various missions, the NIF laser must generate pulses with a wide range of energies, pulse lengths, and temporal pulse shapes. The energy and power of these pulses must be balanced among the 192 beams. Since slight differences in amplifier gains, optical transmission losses, and converter configurations cause the output versus input characteristics to differ among beams, a calibrated computational model of the facility is required to accurately determine the input conditions required for each beam and for each shot. That model must be part of the NIF controls system to provide real-time setup information

within the NIF shot cycle. The LPOM [5,34] has been developed to provide this functionality. The LPOM is run from the control room, where it communicates with a software supervisor, integrating it directly with the NIF ICCS. In addition to generating shot setup information, the LPOM provides an equipment protection function for the NIF operations and archives shot data and analysis for future study. The LPOM may also be run in an off-line mode (not in the control room) for preshot setup and target design studies.

The LPOM maintains a current description of each of the individual NIF subsystems (ILS, main laser, FOA), including component locations, (spatially varying) gains and losses, optical aberrations on each component, aperture and pinhole dimensions, and frequency-converter configurations. It employs an optical physics simulation code, which uses this information both to predict laser performance and to provide inverse problem solution capability. To accomplish its equipment protection function, the LPOM assesses the probability that a calculated shot might initiate optical damage, based on the predicted spatially varying beam fluence, and it prevents the setting up of conditions that would lead to shots outside the standard operating envelope. During the shot setup cycle, it also compares the measured and predicted diagnostic signals and verifies that the laser is functioning as expected. After the shot, the LPOM archives shot data and provides postshot analysis and data visualization functionality.

The LPOM starts the beam setup process based on requests of desired energies and temporal shapes (power) of the beams at a user-specified location. To support both NIF operations and commissioning, the LPOM must enable experimenters to specify energies at a variety of locations along the NIF beamline such as at the target chamber, the roving mirror diagnostics assembly, or the PDS 1ω or 3ω stations. To perform this function, the LPOM incorporates a model of the laser system having enough fidelity to produce realistic and accurate performance calculations. For useful predictions, the laser model must be kept current with the evolving state of the laser system; thus the LPOM is designed to continually acquire data from past shots and update its models. The LPOM uses a detailed energy extraction and propagation code called the VBL [35] to calculate the energetics. VBL models beam propagation in three spatial dimensions plus a number of time slices. Energy extraction is simulated by solving the Frantz–Nodvik equation, including inhomogeneous saturation of neodymium in the laser glass at each transverse position. Optical aberrations, which can significantly influence beam propagation, are included either as measured metrology data or as power spectral density-based simulated phase screens. Nonlinear refractive index (B integral) effects are included as a position-dependent near-field phase push back. Laser beam propagation is modeled as a far-field diffractive phase, which is applied in split step with the preceding near-field effects. Beam focus may be

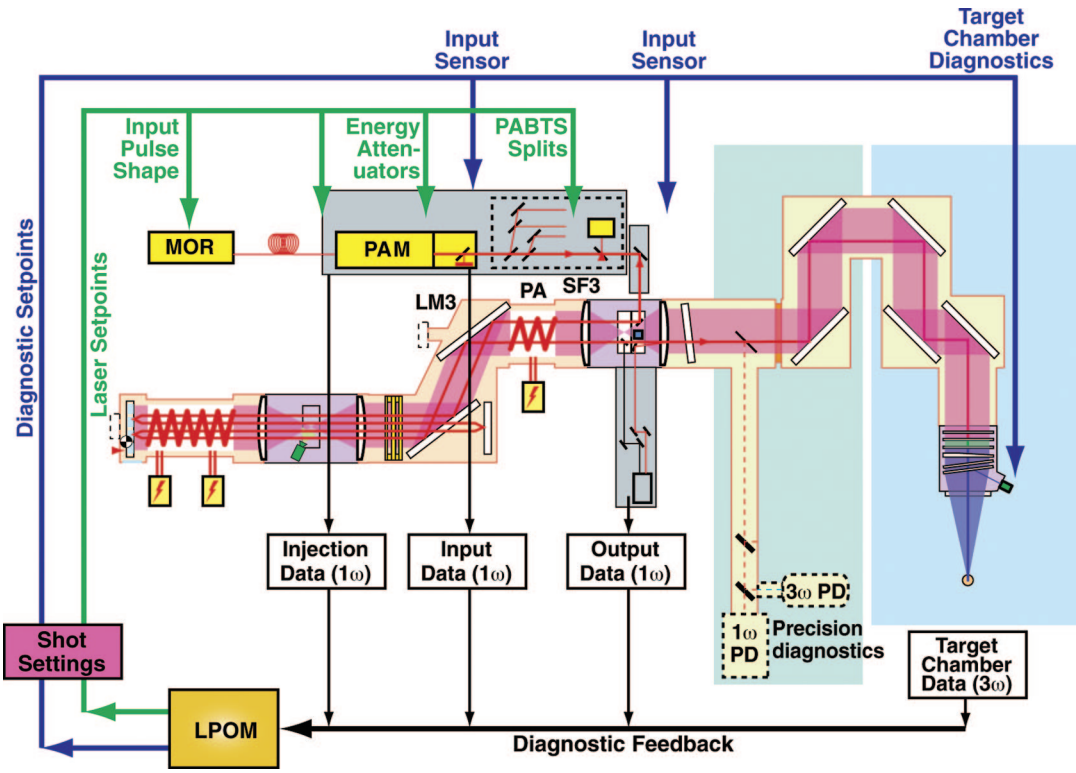

Fig. 41. (Color online) Illustration of the LPOM shot setup process. High-level shot goals and laser configuration data are read by the LPOM and used to generate shot set points for the injection laser system and for diagnostic systems. Shot data is fed back to the LPOM for postshot analysis and for optimization of laser models.

treated either as an applied quadratic near-field phase on the complex field or as a global wavefront curvature using the Talanov transformation. By systematically applying measured metrology information from the many components comprising each NIF beamline, the LPOM has been able to generate predictions that quantitatively agree with measured beam near-field and far-field fluence profiles.

Figure 41 illustrates the LPOM shot setup process. The LPOM reads the goals of an experiment or the NIF shot and information about the proposed laser configuration (e.g., the number of amplifier slabs to be used, the level of flashlamp pumping of the slabs) from the ICCS setup database. From this information, it generates beamline-specific input files for VBL and conducts a series of VBL calculations to self-consistently determine the settings for the injection laser system that will produce the required output temporal pulse. These calculations determine: (1) the optimal MOR temporal pulse shape to meet the shot goals, (2) the attenuator wave-plate settings at the input and output of the PAM four-pass amplifier, and (3) the PABTS wave-plate settings required to properly split the PAM pulse among the four main beamlines. This procedure also predicts the energy and power expected at each diagnostic location, thus determining the attenuation settings necessary for each diagnostic device so that the shot can be accurately measured. These settings are written to the NIF shot database, where they are read by several NIF subsystems (ILS, MOR, and laser diagnostics) to set up the shot.

As part of the setup solution procedure, the LPOM directs VBL to perform an end-to-end simulation of all beamlines involved in the shot. That simulation produces a report to the shot director assessing whether the shot goals are achievable with laser operation inside the standard operating envelope. The LPOM provides additional equipment protection and status by verifying that energies and powers measured during the shot setup cycle match those predicted by the model. Prior to a main laser system shot, the NIF conducts a series of rod shots (shots for which only the ILS amplifiers are energized). The LPOM compares the measured ISP energies, powers, and spatial beam shapes, as well as the energy split among the four beamlines (measured in OSP) to those predicted by the VBL calculation in order to verify that the injection system is performing as expected. If any of these checks fail, the LPOM flags an error to the controls systems, recommends changes to the set points, and requests an additional rod shot.

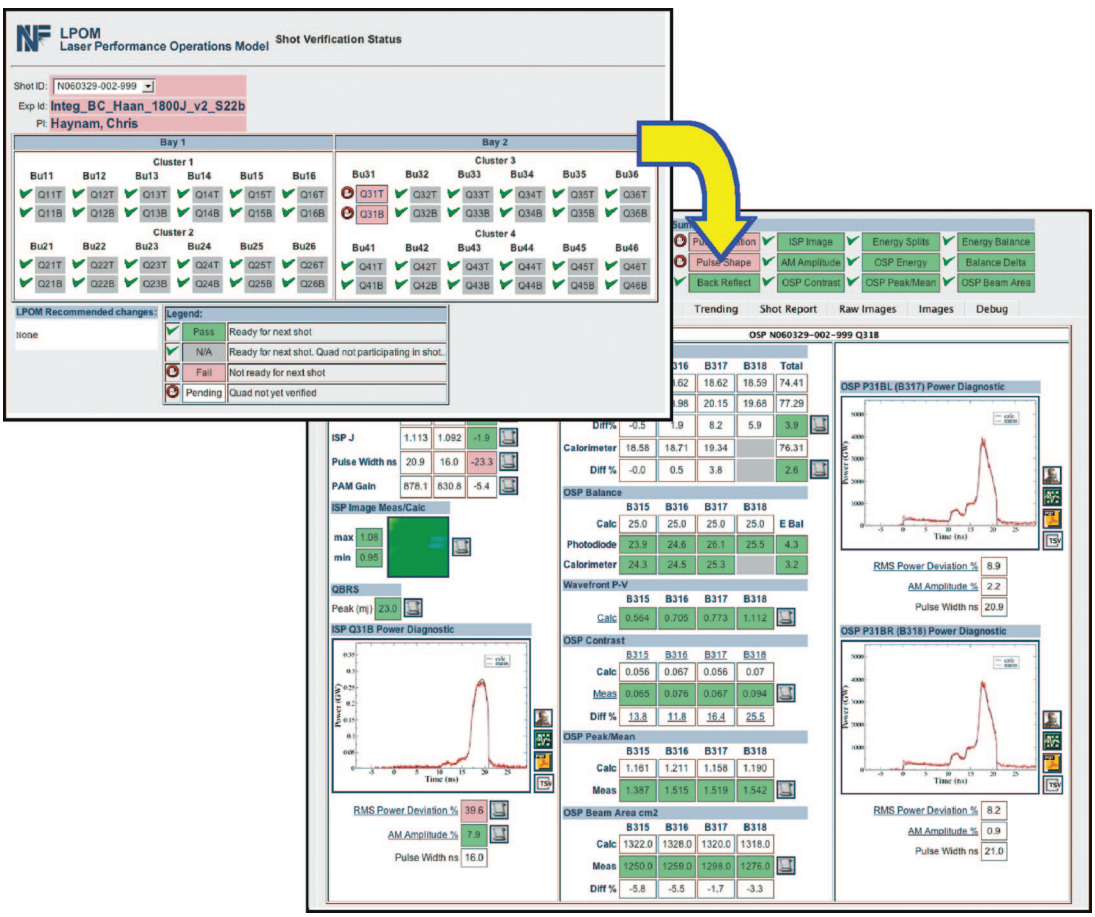

Fig. 42. (Color online) LPOM's shot verification screen provides a top-level performance summary and drill-down capability to detailed shot data.

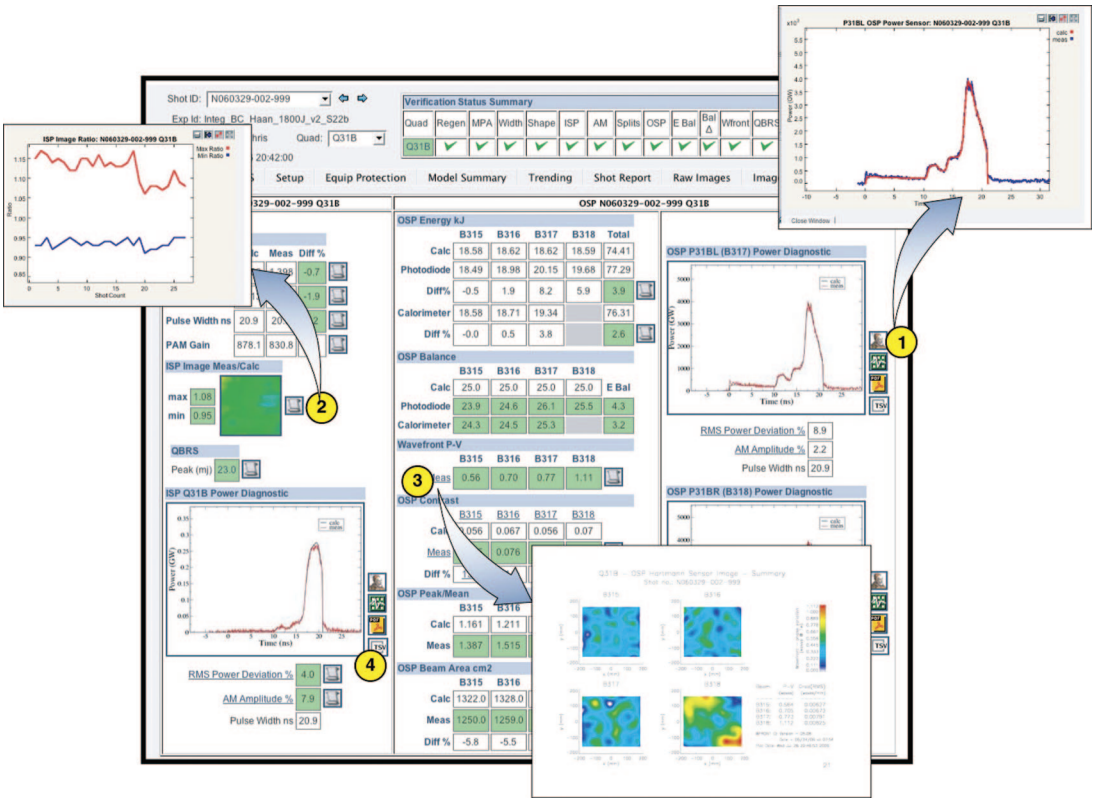

Fig. 43. (Color online) LPOM's web interface provides a powerful suite of data trending and analysis tools.

After a main laser shot, the LPOM performs a more extensive set of analyses to verify the success of the shot and to assure that its models are up to date.

After a shot is conducted, the LPOM shot supervisor directs the LPOM to read the shot data from the ICCS shot database (energetics, near-field, and far-field images) and to perform its postshot analyses. Within a few minutes of the archiving of the raw shot data, the LPOM provides the NIF shot director and the experiment team with a web-based shot report that compares the laser performance metrics (including energetics, near-field beam contrast, residual wavefront distortion, and far-field spot size) with the preshot predictions. It also displays the raw and processed near-field and far-field images, power sensor traces, and trends of selected raw and derived quantities.

These results are presented on the LPOM web browser. The report is organized as a series of linked web pages that can be navigated to provide successive levels of detail, starting with a high-level report on the overall success for each participating quad, and allowing easy access to the underlying analyses. Figure 42 shows a screen capture of the shot verification as presented on the browser, illustrating the ability to easily drill down from the verification status for each participating quad to the more detailed analysis results through embedded hyperlinks and web applets. Figure 43 is another screen capture, illustrating additional data visualization and manipulation capabilities provided through the browser.

Designing, building, commissioning, and testing the NIF laser is the work of many people, all of whom are crucial to the success of the project and deserve our appreciation. We express special thanks to the following: The NIF staff, particularly the operations and commissioning organization, for reviewing test plans, providing practical recommendations, and frequently working extended hours; the engineering team for designing the hardware described in this paper; Phillip Watts and Dustin Froula for their assistance in implementing the PDS spectrometer systems; and Phillip Datte and Jim Kamperschroer for their assistance in the implementation of the temporal diagnostics. Special thanks also to Jack Kelly at the University of Rochester's Laboratory for Laser Energetics for carefully reading the early draft of this paper and making many valuable suggestions.

This work was performed under the auspices of the U.S. Department of Energy, National Nuclear Security Administration by the University of California Lawrence Livermore National Laboratory under contract W-7405-Eng-48.

References

1. G. H. Miller, E. I. Moses, and C. R. Wuest, "The National Ignition Facility," Opt. Eng. **43,** 2841–2853 (2004).
2. M. L. Spaeth, K. R. Manes, C. C. Widmayer, W. H. Williams, P. K. Whitman, M. A. Henesian, I. F. Stowers, and J. Honig, "National Ignition Facility wavefront requirements and optical architecture," Opt. Eng. **43,** 2854–2865 (2004).
3. R. E. Bonanno, "Assembling and installing line-replaceable

units for the National Ignition Facility," Opt. Eng. **43,** 2866–2872 (2004).
4. R. A. Zacharias, N. R. Beer, E. S. Bliss, S. C. Burkhart, S. J. Cohen, S. B. Sutton, R. L. Van Atta, S. E. Winters, J. T. Salmon, M. R. Latta, C. J. Stolz, D. C. Pigg, and T. J. Arnold, "Alignment and wavefront control systems of the National Ignition Facility," Opt. Eng. **43,** 2873–2884 (2004).
5. M. Shaw, W. Williams, R. House, and C. Haynam, "Laser performance operations model," Opt. Eng. **43,** 2885–2895 (2004).
6. E. I. Moses and C. R. Wuest, "The National Ignition Facility: laser performance and first experiments," Fusion Sci. Technol. **47,** 314–322 (2005).
7. J. T. Hunt, K. R. Manes, J. R. Murray, P. A. Renard, R. Sawicki, J. B. Trenholme, and W. Williams, "Laser design basis for the National Ignition Facility," Fusion Technol. **26,** 767–771 (1994).
8. P. J. Wisoff, M. W. Bowers, G. V. Erbert, D. F. Browning, and D. R. Jedlovec, "NIF injection laser system," Proc. SPIE **5341,** 146–155 (2004).
9. J. K. Crane, R. B. Wilcox, N. W. Hopps, D. Browning, M. D. Martinez, B. Moran, F. Penko, J. E. Rothenberg, M. Henesian, C. B. Dane, and L. A. Hackel, "Integrated operations of the National Ignition Facility (NIF) optical pulse generation development system," Proc. SPIE **3492,** 100–111 (1999).
10. M. D. Martinez, K. M. Skulina, F. J. Deadrick, J. K Crane, B. Moran, J. Braucht, B. Jones, S. Hawkins, R. Tilley, J. Crawford, D. Browning, and F. Penko, "Performance results of the high gain, Nd:glass, engineering prototype preamplifier module (PAM) for the National Ignition Facility (NIF)," Proc. SPIE **3611,** 169–180 (1999).
11. B. M. Van Wonterghem, J. R. Murray, J. H. Campbell, D. R. Speck, C. E. Barker, I. C. Smith, D. F. Browning, and W. C. Behrendt, "Performance of a prototype for a large-aperture multipass Nd:glass laser for inertial confinement fusion," Appl. Opt. **36,** 4932–4953 (1997).
12. J. D. Lindl, *Inertial Confinement Fusion: The Quest for Ignition and Energy Gain Using Indirect Drive* (Springer, 1998).
13. J. D. Lindl, "Development of the indirect-drive approach to inertial confinement fusion and the target physics basis for ignition and gain," Phys. Plasmas **2,** 3933–4024 (1995).
14. J. D. Lindl, P. Amendt, R. L. Berger, S. G. Glendenning, S. H. Glenzer, S. W. Haan, R. L. Kaufmann, O. T. Landen, and L. J. Suter, "The physics basis for ignition using indirect-drive targets on the National Ignition Facility," Phys. Plasmas **11,** 339–491 (2004).
15. D. E. Hinkel, S. W. Haan, A. B. Langdon, T. R. Dittrich, C. H. Still, and M. M. Marinak, "National Ignition Facility targets driven at high radiation temperature: ignition, hydrodynamic stability, and laser-plasma interactions," Phys. Plasmas **11,** 1128–1144 (2004).
16. S. W. Haan, M. C. Herrmann, P. A. Amendt, D. A Callahan, T. R. Dittrich, M. J. Edwards, O. S. Jones, M. M. Marinak, D. H. Munro, S. M. Pollaine, J. D. Salmonson, B. K. Spears, and L. J. Suter, "Update on specifications for NIF ignition targets, and their roll up into an error budget," Fusion Sci. Technol. **49,** 553–557 (2006).
17. K. R. Manes and W. W. Simmons, "Statistical optics applied to high-power glass lasers," J. Opt. Soc. Am. A **2,** 528–538 (1984).
18. J. R. Murray, J. R. Smith, R. B. Ehrlich, D. T. Kyrazis, C. W. Thompson, and R. B. Wilcox, "Observation and suppression of transverse stimulated Brillouin scattering in large optics," J. Opt. Soc. Am. B **6,** 2402–2411 (1989).
19. R. Craxton, "High-efficiency tripling schemes for high-power Nd-glass lasers," IEEE J. Quantum Electron. **17,** 1771–1782 (1989).
20. D. Eimerl, J. M. Auerbach, and P. W. Milonni, "Paraxial wave theory of second and third harmonic generation in uniaxial crystals: I. Narrowband pump fields," J. Mod. Opt. **42,** 1037–1067 (1995).
21. W. H. Williams, J. M. Auerbach, M. A. Henesian, K. S. Jancaitis, K. R. Manes, N. C. Mehta, C. D. Orth, R. A. Sacks, M. J. Shaw, and C. C. Widmayer, "Optical propagation modeling for the National Ignition Facility," Proc. SPIE **5341,** 277–278.
22. J. M. Auerbach, P. J. Wegner, S. A. Couture, D. Eimerl, R. L. Hibbard, D. Milam, M. A. Norton, P. K. Whitman, and L. A. Hackel, "Modeling of frequency doubling and tripling with measured crystal spatial refractive-index nonuniformities," Appl. Opt. **40,** 1404–1411 (2001).
23. R. H. Hardin and F. D. Tappert, "Application of the split-step Fourier method to the numerical solution of nonlinear and variable coefficient wave equations," SIAM Rev. **15,** 423 (1973).
24. P. M. Cooley and J. W. Tukey, "An algorithm for the machine computation of complex Fourier series," Math. Comput. **19,** 291–301 (1965).
25. D. H. Munro, S. N. Dixit, A. B. Langdon, and J. R. Murray, "Polarization smoothing in a convergent beam," Appl. Opt. **43,** 6639–6647 (2004).
26. S. Skupsky, R. W. Short, T. Kessler, R. S. Craxton, S. Letzring, and J. M. Soures, "Improved laser beam uniformity using the angular dispersion of frequency-modulated light," J. Appl. Phys. **66,** 3456–3462 (1989).
27. J. E. Rothenberg, "Comparison of beam-smoothing methods for direct-drive inertial confinement fusion," J. Opt. Soc. Am. B **14,** 1664–1671 (1997).
28. J. Goodman, in *Laser Speckle and Related Phenomena,* J. C. Dainty, ed. (Springer-Verlag, 1984), Chap. 2.
29. H. T. Powell, S. N. Dixit, and M. A. Henesian, *Beam Smoothing Capability on the Nova Laser,* LLNL Rep. UCRL-LR-105821-91-1, (Lawrence Livermore National Laboratory, 1990), pp. 28–38.
30. S. N. Dixit, I. M. Thomas, B. W. Woods, A. J. Morgan, M. A. Henesian, P. J. Wegner, and H. T. Powell, "Random phase plates for beam smoothing on the Nova laser," Appl. Opt. **32,** 2543–2554 (1993).
31. S. N. Dixit, I. M. Thomas, M. R. Rushford, R. Merrill, M. D. Perry, H. T. Powell and K. A. Nugent, "Kinoform phase plates for tailoring focal plane intensity profiles," LLNL Rep. UCRL-LR-105821-94-4, (Lawrence Livermore National Laboratory, 1994), pp. 152–159.
32. S. N. Dixit, M. D. Feit, M. D. Perry, and H. T. Powell, "Designing fully continuous phase plates for tailoring focal plane irradiance profiles," Opt. Lett. **21,** 1715–1717 (1996).
33. J. A. Menapace, S. N. Dixit, F. Y. Génin, and W. F. Brocious, "Magnetorheological finishing for imprinting continuous phase plate structure onto optical surfaces," Proc. SPIE **5273,** 220–230 (2003).
34. M. Shaw, W. Williams, K. Jancaitis, C. Widmayer, and R. House, "Performance and operational modeling of the National Ignition Facility," at the *International Symposium on Optical Science and Technology* (2003).
35. C. A. Haynam, R. A. Sacks, and M. J. Shaw, "Computational modeling in support of the National Ignition Facility operations," presented at the *8th International Conference on Accelerator and Large Experimental Physics and Controls Systems* (ICALEPS, 2001).